Quantum nonlinear optics without photons

Roberto Stassi,[1] Vincenzo Macrì,[1,2] Anton Frisk Kockum,[1] Omar Di Stefano,[1] Adam Miranowicz,[1,3]
Salvatore Savasta,[1,2] and Franco Nori[1,4]

[1]*Center for Emergent Matter Science, RIKEN, Saitama 351-0198, Japan*
[2]*Dipartimento di Scienze Matematiche e Informatiche, Scienze Fisiche e Scienze della Terra, Università di Messina, I-98166 Messina, Italy*
[3]*Faculty of Physics, Adam Mickiewicz University, PL-61-614 Poznan, Poland*
[4]*Physics Department, University of Michigan, Ann Arbor, Michigan 48109-1040, USA*

Spontaneous parametric down-conversion is a well-known process in quantum nonlinear optics in which a photon incident on a nonlinear crystal spontaneously splits into two photons. Here we propose an analogous physical process where one excited atom directly transfers its excitation to a pair of spatially separated atoms with probability approaching 1. The interaction is mediated by the exchange of *virtual* rather than *real* photons. This nonlinear atomic process is coherent and reversible, so the pair of excited atoms can transfer the excitation back to the first one: the atomic analog of sum-frequency generation of light. The parameters used to investigate this process correspond to experimentally demonstrated values in ultrastrong circuit quantum electrodynamics. This approach can be extended to realize other nonlinear interatomic processes, such as four-atom mixing, and is an attractive architecture for the realization of quantum devices on a chip. We show that four-qubit mixing can efficiently implement quantum repetition codes and, thus, can be used for error-correction codes.

I. INTRODUCTION

It is highly desirable to couple distant qubits for quantum-information applications [1,2]. One implementation of such a quantum bus has been demonstrated using microwave photons confined in a transmission-line cavity to couple two superconducting qubits on opposite sides of a chip [3]. Interestingly, the interaction between the two qubits is mediated by the exchange of *virtual* rather than *real* photons, avoiding cavity-induced losses [3]. The effective qubit-qubit interaction is the result of the exchange of virtual photons with the cavity and gives rise to a qubit-qubit avoided level crossing. At the minimum splitting, the eigenstates of the system are symmetric and antisymmetric superpositions of the two qubit states $|e,g\rangle$ and $|g,e\rangle$, where $|g\rangle$ ($|e\rangle$) labels the ground (excited) state of the qubits. When the two qubits have the *same* transition energy, an excitation in one qubit can be coherently transferred to the other qubit by virtually becoming a photon in the cavity [3]. When the qubits have different transition energies, the interaction is effectively turned off. The absence of cavity-induced losses, due to the virtual nature of the quantum bus, is useful especially in the presence of intrinsically lossy interaction channels. For example, it has been shown theoretically [4] that virtual plasmon polaritons in realistic one-dimensional subwavelength waveguides are excellent candidates to act as mediators for achieving a high degree of entanglement between two distant qubits.

Here we propose a generalization of the qubit-qubit coupling via virtual bosons, which enables the interaction of multiple ($N > 2$) spatially separated qubits with *different* transition frequencies. For example, we show that, in analogy to the frequency-mixing processes of nonlinear optics, one qubit of given transition frequency ω_3 can coherently transfer its excitation to a pair of qubits (1 and 2) if $\omega_1 + \omega_2 = \omega_3$. The results presented here open the way to *nonlinear optical processes without real photons*. Instead, virtual photons, which are *not* subject to cavity-induced losses and decoherence,

drive the interaction between spatially separated and non-degenerate qubits. While the qubit-qubit resonant excitation transfer can be well described by the Tavis-Cummings (TC) model [5], the process proposed here cannot be described without including the counter-rotating terms in the atom-field interaction Hamiltonian, neglected in the TC model. Although the Hamiltonian of a realistic atom-cavity system contains counter-rotating terms (allowing the simultaneous creation or annihilation of an excitation in both atom and cavity mode), these terms can be safely neglected for coupling rates that are small with respect to the atomic transition frequency and the cavity-mode resonance frequency. However, when the coupling rate increases, the counter-rotating terms start to play an important role, giving rise to a new regime of cavity quantum electrodynamics (QED). This ultrastrong-coupling (USC) regime was recently realized in a variety of solid-state systems [6–22]. This opens the door to the study of the physics of virtual processes that do not conserve the number of excitations [23–31]. Recently, it has been shown that, through higher-order processes where virtual photons are created and annihilated, an effective deterministic coupling between two states of such a system can be created giving rise to new effects such as multiphoton Rabi oscillations [32–34] and a single photon exciting multiple atoms [35]. Moreover, it has been shown that almost any analog of nonlinear optical processes is feasible [36] without the need for high-intensity driving fields. The results presented here go one remarkable step forward, beyond Ref. [36], showing that nonlinear optical processes involving only atoms, without the need for *real* photons, are also feasible.

In quantum nonlinear optics, the effective interaction Hamiltonian for a three-mode parametric process can be written as [37]

$$\hat{V}_c^{(3)} = K^{(3)} \, \hat{a}_1^\dagger \hat{a}_2^\dagger \hat{a}_3 + \text{H.c.}, \tag{1}$$

where $\hat{a}_i$ and $\hat{a}_i^\dagger$ are photon destruction and creation operators for the ith mode, and $K^{(3)}$ is a constant describing the strength of the nonlinear interaction. This Hamiltonian describes well-known nonlinear optical processes, such as sum-frequency generation and spontaneous parametric down-conversion. The latter process is used especially as a source of entangled photon pairs and of single photons. Analogously, the process proposed here can be described by the following effective three-qubit Hamiltonian,

$$\hat{V}^{(3)} = J^{(3)} \hat{\sigma}_+^{(1)} \hat{\sigma}_+^{(2)} \hat{\sigma}_-^{(3)} + \text{H.c.}, \tag{2}$$

where $\hat{\sigma}_\pm^{(i)}$ are the raising (+) and lowering (−) Pauli operators for qubit i, and the effective coupling $J^{(3)}$, as we show, can be calculated by perturbation theory. This three-body effective interatomic interaction describes three-qubit-mixing (3QM) processes as the coherent and reversible transfer of an excitation from one qubit to two spatially separated qubits or vice versa. We show that four-qubit mixing (4QM), described by the effective Hamiltonian

$$\hat{V}_I^{(4)} = J^{(4)} \hat{\sigma}_-^{(1)} \hat{\sigma}_-^{(2)} \hat{\sigma}_+^{(3)} \hat{\sigma}_+^{(4)} + \text{H.c.}, \tag{3}$$

is also possible, where $J^{(4)}$ is the effective coupling strength. The four-wave mixing of light [38] arises from third-order optical nonlinearities. In typical cases, a photon of frequency ω_4 results from the annihilation of photons at ω_1 and ω_2 and the stimulated emission of one at ω_3 with $\omega_4 + \omega_3 = \omega_1 + \omega_2$. The process can also be spontaneous, occurring even in the absence of stimulation at ω_3. The effective potential in Eq. (3) enables the simultaneous excitation transfer from qubits 1 and 2 to qubits 3 and 4 when the qubit transition frequencies satisfy the relation $\omega_1 + \omega_2 = \omega_3 + \omega_4$, which is an interatomic scattering process without the presence of real photons. This process is the qubit analog of the spontaneous four-wave mixing of light (see, e.g., Ref. [39]). In the following we refer to it as type-I 4QM in order to distinguish it from a different type of 4QM (type II), achievable in our system in the USC regime when $\omega_4 = \omega_1 + \omega_2 + \omega_3$. This latter process can efficiently perform quantum repetition codes after a proper evolution time. We show that such spontaneous evolution of the system can be used for error-correction codes [40,41] for encoding, decoding, and error-syndrome detection.

Note that the framework proposed here is different from nonlinear atom optics [42], where the atomic center-of-mass degree of freedom is involved. Coherent matter waves in the form of Bose-Einstein condensates have led to the development of nonlinear and quantum atom optics, where atomic waves are manipulated in a manner analogous to the manipulation of light [43,44]. For example, coherent four-wave mixing (in which three sodium matter waves of differing momenta mix to produce a fourth wave with another momentum) has been demonstrated experimentally [45].

It has also been shown that a system of trapped ions can be used to implement spin models with three-body interactions [46]. However, in contrast to the framework proposed here, where the effective interaction is enforced by the field quantum vacuum only, in trapped ions the effective three-spin interactions are induced by external lasers.

As we show below, the effective Hamiltonians in Eqs. (2) and (3) can be derived from a generalized Dicke Hamiltonian

[47], describing three or more qubits interacting with the same oscillator (cavity mode). The interaction Hamiltonian also includes a longitudinal coupling term [48], which arises when the inversion symmetry of the potential energy of the artificial atoms (qubits) is broken [49,50].

II. RESULTS

A. Description of the system

Here we examine a quantum system of N two-level atoms (with possible symmetry-broken potentials) coupled to a single-mode resonator. The Hamiltonian describing this system is (e.g., Refs. [10,28])

$$\hat{H}_0 = \hat{H}_q + \hat{H}_c + \hat{V}, \tag{4}$$

where (using $\hbar = 1$) $\hat{H}_q = \sum_i (\omega_i/2) \hat{\sigma}_z^{(i)}$ and $\hat{H}_c = \omega_c \hat{a}^\dagger \hat{a}$ describe the qubit and cavity Hamiltonians, respectively, in the absence of interaction. The qubits-cavity interaction is

$$\hat{V} = \hat{X} \sum_i \lambda_i \big(\cos\theta_i \, \hat{\sigma}_x^{(i)} + \sin\theta_i \, \hat{\sigma}_z^{(i)} \big), \tag{5}$$

where $\hat{X} = \hat{a} + \hat{a}^\dagger$, $\hat{\sigma}_x^{(i)}$ and $\hat{\sigma}_z^{(i)}$ are Pauli operators for the ith qubit, λ_i are the coupling rates of each qubit to the cavity mode, and θ_i are parameters determining the relative contribution of the transverse and longitudinal couplings. For $\theta_i = 0$, the parity of qubit i is conserved. For flux qubits, the angles θ_i, as well as the transition frequencies ω_i, can be continuously and individually tuned by changing the external flux biases [10,48]. In contrast to the TC model, the Hamiltonian in Eq. (4) explicitly contains counter-rotating terms of the form $\hat{\sigma}_+^{(i)} \hat{a}^\dagger$, $\hat{\sigma}_-^{(i)} \hat{a}$, $\hat{\sigma}_z^{(i)} \hat{a}^\dagger$, and $\hat{\sigma}_z^{(i)} \hat{a}$. The first (second) term creates (destroys) two excitations, while the third (fourth) term creates (destroys) one excitation. Equation (4) represents the simplest Hamiltonian describing the interaction of N atoms (with possible symmetry-broken potentials) with the electromagnetic field of a cavity beyond the rotating-wave approximation (RWA). This model is well suited for describing atoms with very large anharmonicity, such as flux qubits. However, we expect that the results presented below also apply, at least qualitatively, to more general atom-cavity systems when additional atomic levels are involved.

In the case of two qubits ($i = 1,2$), dropping the counter-rotating terms, considering the dispersive regime ($|\Delta_i| = |\omega_i - \omega_c| \gg \lambda_i$), and applying second-order perturbation theory, it is possible to derive from the atom-cavity interaction Hamiltonian [see Eq. (4)] the following effective interaction Hamiltonian [3,51]:

$$\hat{V}^{(2)} = J^{(2)} \hat{\sigma}_+^{(2)} \hat{\sigma}_-^{(1)} + \text{H.c.}, \tag{6}$$

where $J^{(2)} = \lambda_1 \lambda_2 (1/\Delta_1 + 1/\Delta_2)/2$. In this regime, no energy is exchanged between the qubits and the cavity. This qubit-qubit interaction is the result of virtual exchange of photons with the cavity. It gives rise to a qubit-qubit avoided level crossing when the transition energy of one of the two qubits is continuously tuned across the fixed transition energy of the other. When the qubits are degenerate, an excitation in one qubit can be transferred to the other qubit by virtually becoming a photon in the cavity. However, when the qubits are nondegenerate, $|\omega_1 - \omega_2| \gg J^{(2)}$, this process does not

conserve energy and, therefore, the interaction is effectively turned off.

The dispersive-regime condition $|\Delta_i| = |\omega_i - \omega_c| \gg \lambda_i$ is necessary to enable the virtual exchange of photons. Moreover, in order to ensure that only a negligible population of real photons is present, the atom-cavity detuning has to be much larger than the atomic and photonic decoherence rates.

Throughout this paper, we consider a single-mode optical resonator. Many circuit-QED experiments use an *LC* resonator, which only has a single mode. When additional modes are considered, the dispersive-regime conditions have to hold for all the modes. Defining $|\Delta_{i,n}| = |\omega_i - \omega_{c,n}|$, where $\omega_{c,n}$ is the nth mode frequency, the conditions are $|\Delta_{i,n}| \gg \lambda_i$ and $|\Delta_{i,n}| \gg \kappa_n$, where κ_n is the decay rate of the nth mode. If these conditions are satisfied, following the procedure of Ref. [51], it is straightforward to find $J^{(2)} = \sum_n [\lambda_{1,n} \lambda_{2,n}(1/\Delta_{1,n} + 1/\Delta_{2,n})/2]$. This series is expected to converge, owing to the suppression of light-matter coupling $\lambda_{i,n}$ at high frequencies (see, e.g., Ref. [52]). If the lowest-frequency mode is not too far detuned from the atomic transition frequencies, and the modes are well separated spectrally, only the lowest-frequency mode will provide a significant contribution. The experimental results shown in Ref. [3], obtained using a $\lambda/4$ coplanar waveguide resonator, are very well described considering a single mode, since higher-energy modes are too far off resonance to give a significant contribution. Analogous considerations apply to the processes described here. On the contrary, in a large cavity ($l \gg \lambda_i$) or in a transmission line, the modes constitute either a quasicontinuum or a continuum, and the single-mode description adopted here does not work. In this case, one possibility to realize a qubit-qubit interaction mediated by virtual photons is to consider atoms with transition frequencies outside the frequency bandwidth of the photonic system.

In the following, we show how the Hamiltonian in Eq. (4) can also give rise to effective qubit-qubit interactions involving more than two qubits. Specifically, we consider nonlinear interatomic processes involving nondegenerate qubits, such as 3QM and 4QM.

B. Three-qubit mixing

Here we consider three nondegenerate qubits of transition frequencies $\omega_1 \neq \omega_2 \neq \omega_3$ coupled to a cavity mode [see Fig. 1(a)]. Figure 1(b) shows the energy levels for the excited lowest-energy states as a function of the frequency of qubit 3, obtained by numerically diagonalizing Eq. (4). For each value of ω_3, the energy scale is chosen such that the ground-state energy is equal to zero. All the parameters are provided in terms of a fixed reference frequency ω_0. We assume that qubits 1 and 2 are ultrastrongly coupled to the cavity mode, while the coupling strength of qubit 3 with the cavity mode is lower. We used $\lambda_3/\omega_0 = 5 \times 10^{-3}$, $\lambda_1/\omega_0 = \lambda_2/\omega_0 = 0.13$, $\theta_i = \pi/6$ for all the qubits, $\omega_1/\omega_0 = 0.4$, $\omega_2/\omega_0 = 0.6$, and $\omega_c = \omega_0 + 2.5\lambda_1$. The lowest-energy horizontal line (with $\omega/\omega_0 \approx 0.4$) corresponds to the excitation of qubit 1. We indicate this state as $|\psi_1\rangle = |e,g,g,0\rangle$, where the first three entries in the ket describe the states of the three qubits and the last entry describes the cavity-mode state. We observe that this eigenstate, corresponding to the excitation of the *physical*
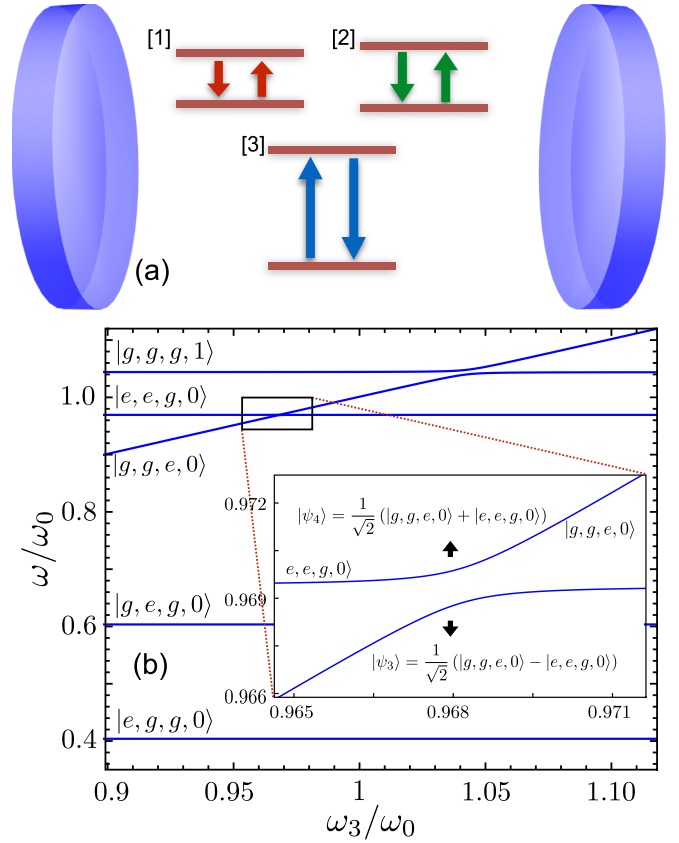

FIG. 1. (a) Schematic representation of three nondegenerate qubits interacting with the electromagnetic field of a cavity. (b) Lowest-energy levels, indicated with ω ($\hbar = 1$), of the system constituted by three qubits interacting with a cavity mode as a function of the normalized frequency of qubit 3, obtained by numerically diagonalizing the Hamiltonian in Eq. (4). The transition frequencies of the other two qubits, as well as the resonance frequency of the cavity mode, are kept fixed. All the parameters used here are specified in the text. The enlarged view of the boxed *apparent* crossing in the inset displays a clear anticrossing level splitting. When the splitting is at its minimum, the eigenstates of the system are approximately symmetric and antisymmetric superpositions of the states $|g,g,e,0\rangle$ and $|e,e,g,0\rangle$.

qubit 1, can differ from the bare state $|e,g,g,0\rangle_b$, describing the excitation of qubit 1 in the absence of its interaction with the cavity mode (see, e.g., Ref. [53]). Owing to the dressing effects induced by the counter-rotating terms in the interaction Hamiltonian, differences between bare and physical states occur for all the energy eigenstates. The second horizontal line (with $\omega/\omega_0 \approx 0.6$) corresponds to $|\psi_2\rangle = |g,e,g,0\rangle$. A signature of the discussed dressing is the slight frequency shift occurring between the bare qubit frequencies ω_2 and ω_3 and the two lowest-energy (horizontal) levels displayed in Fig. 1(b) (with $\omega/\omega_0 \approx 0.4$ and 0.6) corresponding to the *physical* transition frequencies of qubits 1 and 2 (in the presence of the interaction with the cavity mode), respectively. In the region much below the first (apparent) crossing ($\omega_3/\omega_0 < 0.95$), the third level corresponds to $|\psi_3\rangle = |g,g,e,0\rangle$, as can also be inferred from its linear dependence on ω_3. In the same frequency region, the fourth level (with $\omega/\omega_0 \approx 0.97$)

corresponds to the simultaneous excitation of qubits 1 and 2, $|\psi_4\rangle = |e,e,g,0\rangle$, while the fifth level (with $\omega/\omega_0 \approx 1.04$) corresponds to the one-photon state $|\psi_5\rangle = |g,g,g,1\rangle$. When increasing ω_3/ω_0, the energy level associated with $|g,g,e,0\rangle$ rises, and it reaches the energy levels corresponding to $|e,e,g,0\rangle$ and $|g,g,g,1\rangle$. When the (dressed) energy of qubit 3 approaches that of the cavity mode, a clear anticrossing can be observed. This is the ordinary vacuum Rabi splitting, which can also be reproduced within the RWA. When this splitting is at its minimum, the eigenstates of the system are the symmetric and antisymmetric superpositions of the states $|g,g,g,1\rangle$ and $|g,g,e,0\rangle$, as confirmed by numerical calculations. More interestingly, Fig. 1(b) also displays an apparent crossing at lower energy when $\omega_3 \simeq \omega_1 + \omega_2$ ($\approx 0.4 + 0.6$). The enlarged view in the inset shows that this is actually an anticrossing level splitting. When this splitting is at its minimum [see inset in Fig. 1(b)], the two system eigenstates $|\psi_{3,4}\rangle$ are, respectively, the antisymmetric and symmetric superpositions of the states $|g,g,e,0\rangle$ and $|e,e,g,0\rangle$. This avoided level crossing indicates a coherent coupling, which does not conserve the number of excitations, of the three spatially separated qubits.

The origin of this coupling can be understood using time-dependent fourth-order perturbation theory, identifying the resulting transition amplitude between the initial state $|i\rangle \equiv |e,g,g,0\rangle_{\rm b}$ and the final state $|f\rangle \equiv |g,e,e,0\rangle_{\rm b}$ (or vice versa) with the effective coupling strength determining this level splitting. According to fourth-order perturbation theory, this coupling can be expressed as [36]

$$\lambda_{\rm eff} = \sum_{n,m,k} \frac{V_{fn} V_{nm} V_{mk} V_{ki}}{(E_i - E_n)(E_i - E_m)(E_i - E_k)}, \qquad (7)$$

where $V_{n,m} = \langle n|\hat{V}|m\rangle$. Although the initial and final states do not contain photons, the coupling is determined by the interaction of the qubits with the cavity field. States with nonzero photon number play a role only as intermediate levels ($|n\rangle$, $|m\rangle$, and $|k\rangle$) reached by virtual transitions (see diagrams in Appendix B). The two states $|i\rangle$ and $|f\rangle$ are connected via a fourth-order process and there are no lower-order contributions. There are 48 paths connecting the states to this order, as shown in Fig. 8. These paths clearly show that the three qubits are connected by a nonlinear optical process involving *only* virtual photons. This analysis has been performed for two-level atoms, which is a good approximation for flux qubits where the next higher level can be energetically very far (see, e.g., Ref. [54]). Of course, additional paths must be taken into account for multilevel systems. The resulting effective coupling between the states $|g,g,e,0\rangle$ and $|e,e,g,0\rangle$ can be described by the effective Hamiltonian in Eq. (2), where $J^{(3)} = \lambda_{\rm eff}$ [corresponding to half the minimum level splitting shown in the inset in Fig. 1(b)].

The analytical expression obtained from Eq. (7), which considers the 48 contributions, is very cumbersome. However, it can be simplified considerably if we assume $\lambda_1 = \lambda_2 = \lambda_3 = \lambda$ and $\omega_1 = \omega_2 = \omega_3/2$. In this case, the final result is

$$J^{(3)} = \frac{64\lambda^4 \omega_c^2 (4\omega_c^2 - 7\omega_3^2) \sin\theta \cos^3\theta}{\omega_3 (\omega_3^2 - \omega_c^2)(\omega_3^2 - 4\omega_c^2)^2}. \qquad (8)$$
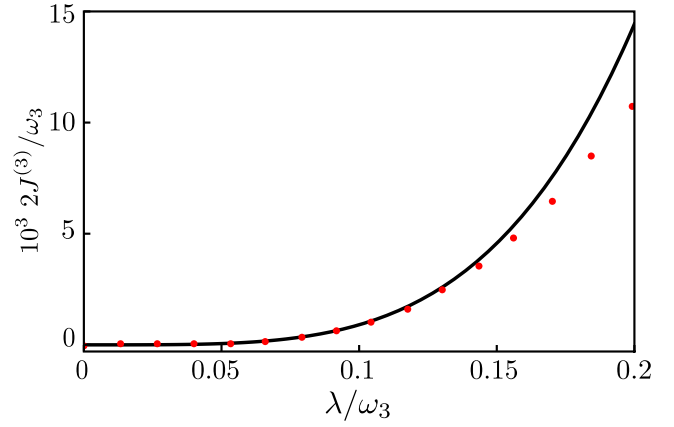

FIG. 2. Comparison between the numerically calculated normalized effective Rabi splitting (points) corresponding to $J^{(3)}$ in Appendix B and the corresponding calculations using fourth-order perturbation theory (continuous black curve), as a function of the normalized interaction strength λ/ω_3.

We note that the effective coupling becomes zero when $\omega_c = \frac{\sqrt{7}}{2}\omega_3$. It is not easy to see how the interference between the 48 paths becomes destructive for this particular value of ω_c. Looking at the denominator of Eq. (8), we see that $J^{(3)} \to \infty$ when $\omega_c \to \omega_3$ or $\omega_c \to \frac{1}{2}\omega_3$, i.e., when the cavity becomes resonant with one of the qubits. Perturbation theory is not valid around those points. We also note that the coupling, also in the unsimplified general case, is proportional to $\sin\theta\cos^3\theta$, which implies that the maximum coupling is achieved when $\theta = \pi/6$. Figure 2 displays a comparison of the magnitudes of the effective Rabi splitting $2J^{(3)}/\omega_3$ obtained analytically [Eq. (8)] via fourth-order perturbation theory (black continuous curve) and by numerical diagonalization of the Hamiltonian in Eq. (4), as a function of the normalized interaction strength λ/ω_3 ($\lambda = \lambda_{1,2,3}$). The other parameters are the same as those used to obtain the results in Fig. 1. The agreement is very good for normalized interaction strengths $\lambda/\omega_3 \lesssim 0.15$. Figure 2 shows that an effective coupling rate well beyond typical decoherence rates of circuit-QED systems (see, e.g., Ref. [55]) can be obtained already at a coupling strength $\lambda/\omega_3 \sim 0.1$.

In order to demonstrate the simultaneous excitation transfer from qubit 3 to qubits 1 and 2, we fix $\omega_3 \simeq \omega_1 + \omega_2$, so that the system is at its minimum-level splitting [see inset in Fig. 1(b)]. The minimum occurs when the transition energy of the dressed qubit 3 is equal to the energy level corresponding to the simultaneous excitation of the dressed qubits 1 and 2. We study the dynamics after initial preparation of the system in the symmetric superposition of the eigenstates associated with the two split energy levels: $(|\psi_3\rangle + |\psi_4\rangle)/\sqrt{2} = |g,g,e,0\rangle$, corresponding to the excitation of the dressed qubit 3. The system can be prepared in this state by directly exciting the detuned qubit 3 by sending a π electromagnetic pulse, followed by a flux shift that brings the qubit into resonance (minimum splitting). Another possibility is to start with qubit 3 already on resonance and excite it by a π pulse much faster than $\pi/J^{(3)}$.

The influence of the cavity-field damping and atomic decay on the process can be studied by the master-equation
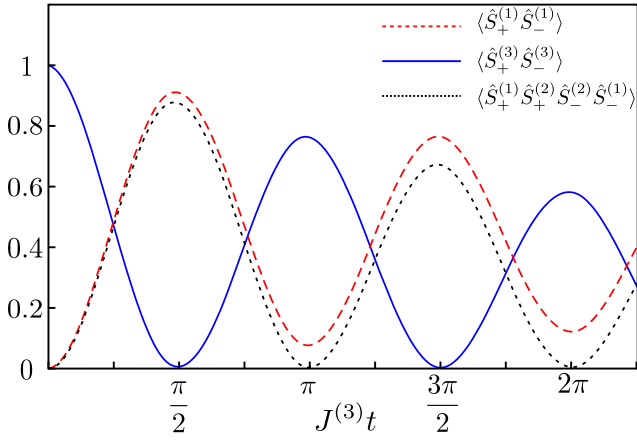
FIG. 3. Time evolution of the mean excitation probabilities of qubits 1 and 3, $\langle \hat{S}_+^{(1)} \hat{S}_-^{(1)} \rangle$ and $\langle \hat{S}_+^{(3)} \hat{S}_-^{(3)} \rangle$, and of the two-qubit correlation function $\langle \hat{S}_+^{(1)} \hat{S}_+^{(2)} \hat{S}_-^{(2)} \hat{S}_-^{(1)} \rangle$. The initial state is $|g,g,e,0\rangle$.

approach in the dressed picture [56,57]. We consider the system interacting with zero-temperature baths. The master equation is obtained by using the Born-Markov approximation without the post-trace RWA [33]. We study the dynamics of the relevant system population and correlation functions by introducing the dressed-qubit lowering and raising operators $\hat{S}_-^{(i)}$ and $\hat{S}_+^{(i)} = (\hat{S}_-^{(i)})^\dagger$. They are a direct generalization of $\hat{\sigma}_-^{(i)}$ and $\hat{\sigma}_+^{(i)}$. For qubit 1,

$$\hat{S}_-^{(1)} = \sum_{n=0}^{\infty} \sum_{\alpha,\beta=g}^{e} |g,\alpha,\beta,n\rangle\langle e,\alpha,\beta,n|. \tag{9}$$

In the absence of interaction, when $|p,q,r,n\rangle$ are bare states, the operators $\hat{S}_-^{(i)}$ coincide with the usual lowering Pauli operators $\hat{\sigma}_-^{(i)}$. Figure 3 displays the time evolution of the mean excitation probability $\langle \hat{S}_+^{(i)} \hat{S}_-^{(i)} \rangle$ of qubits 1 and 3 (the dynamics of qubit 1 coincides with that of qubit 2), as well as that of the two-qubit correlation function $\langle \hat{S}_+^{(1)} \hat{S}_+^{(2)} \hat{S}_-^{(2)} \hat{S}_-^{(1)} \rangle$. The initial state is $|g,g,e,0\rangle = (|\psi_3\rangle + \psi_4\rangle)/\sqrt{2}$. The parameters are those used to obtain the energy levels in Fig. 1(b). For the decay rates of the qubit (γ) and the cavity (κ), we used $\gamma = \kappa = 3 \times 10^{-5}\omega_0$. Quantum Rabi oscillations, showing the reversible excitation exchange between qubit 3 and qubits 1 and 2, can be clearly observed. Note that, during the time evolution displayed in Fig. 3, the photon population (not shown) reaches a maximum value $\sim 1.5 \times 10^{-2}$. This small population decreases rapidly when increasing the detuning Δ_3 between the cavity mode and qubit 3. We also checked that increasing the photon damping, provided that $\kappa \lesssim 2\Delta_3$, does not affect the displayed dynamics. After half a Rabi period ($t = \pi/2J^{(3)}$), the excitation is fully transferred from qubit 3 to qubits 1 and 2, which reach their maximum excitation probability. The presence of damping prevents $\langle \hat{S}_+^{(1)} \hat{S}_-^{(1)} \rangle$ from reaching 1. We observe that the single-qubit excitations and the two-qubit correlation function $\langle \hat{S}_+^{(1)} \hat{S}_+^{(2)} \hat{S}_-^{(2)} \hat{S}_-^{(1)} \rangle$ almost coincide at early times. This almost-perfect two-qubit correlation is a clear signature of the joint excitation of qubits 1 and 2: if one qubit becomes excited, the probability that the other one is excited is also very close to 1. However, as expected, the

two-qubit correlation is more fragile to losses. We also observe that, at time $t = \pi/4J^{(3)}$, this process spontaneously gives rise to the maximally entangled three-qubit state $(|g,g,e\rangle - i|e,e,g\rangle)/\sqrt{2}$ when damping can be neglected (the factorized photonic vacuum state has been disregarded). This state is the Greenberger-Horne-Zeilinger (GHZ) state, up to a local transformation.

We observe that, during the time evolution displayed in Fig. 3, the photon population (not shown) reaches a maximum value of $\sim 1.5 \times 10^{-2}$. This small population decreases rapidly when increasing the detuning Δ_3 between the cavity mode and qubit 3. We also checked that increasing the photon damping, provided that $\kappa \lesssim 2\Delta_3$, does not affect the displayed dynamics. This result shows that the 3QM process is not influenced by the cavity-loss rate κ, owing to the negligible probability to have real photons in the cavity. This result, however, does not imply a total immunity to losses of the quantum bus. For example, if an impurity atom, almost resonant with the transition energy of qubit 3, is present inside the bus, the excitation would be partly transferred to the impurity atom.

This 3QM offers also the possibility to encode an arbitrary qubit state $a|g\rangle + b|e\rangle$ into a two-qubit entangled state so that $(a|g\rangle + b|e\rangle)|g\rangle|g\rangle \to |g\rangle(a|g\rangle|g\rangle - ib|e\rangle|e\rangle)$. This operation can be realized by just letting the system evolve spontaneously for a time $t = \pi/2J^{(3)}$.

C. Four-qubit mixing

Here we consider four nondegenerate qubits coupled to a cavity mode in the dispersive regime and investigate the 4QM process. Figure 4 shows the energy levels for the lowest-energy excited states as a function of the frequency of qubit 1, obtained by numerically diagonalizing the Hamiltonian in Eq. (4). Also in this case, for each value of ω_1, the energy scale is chosen such that the ground-state energy is equal to zero. All the values are provided in terms of a fixed reference frequency ω_0. We used $\lambda_i/\omega_0 = 0.15$ and $\theta_i = \pi/6$ for all the qubits. We also set the transition frequencies of qubits 2, 3, and 4 as $\omega_2/\omega_0 = 0.4$, $\omega_3/\omega_0 = 0.55$, and $\omega_4/\omega_0 = 0.7$, and the resonance frequency of the cavity mode as $\omega_c/\omega_0 = 1.4$.

The figure displays several *apparent* level crossings and anticrossings, corresponding to different kinds of normal-mode couplings. The avoided level crossings indicated by the red circles originate from two-qubit resonant interactions described by the effective Hamiltonian in Eq. (6). In the time domain, this type of interaction leads to two-qubit mixing (2QM). The *apparent* level crossings labeled by the orange triangles give rise to 3QM. For example, the lowest-energy orange triangle (at $\omega/\omega_0 \simeq 0.6$) marks the coupling between the states $|g,g,e,g,0\rangle$ and $|e,e,g,g,0\rangle$. The stars in the higher-energy region describe the coupling of a single photon to two (open star) or three (solid star) qubits, studied in Ref. [35]. Type-I 4QM processes are denoted by open squares. An enlarged view of the *apparent* crossing ($\boxtimes$) in Fig. 4 is plotted in Fig. 5(a). There, an anticrossing level splitting of $\sim 10^{-3}\omega_0$ can be observed. When the splitting is at its minimum, the two system eigenstates are the symmetric and antisymmetric superpositions of the states $|e,g,g,e,0\rangle$ and $|g,e,e,g,0\rangle$. This avoided level crossing is the signature of a four-qubit coherent coupling.
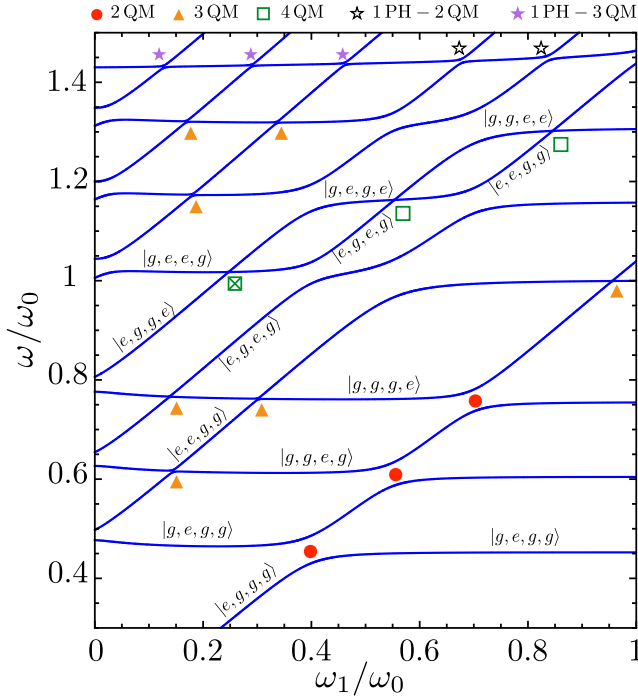
FIG. 4. Four nondegenerate qubits dispersively coupled to a cavity mode at higher energy. Lowest-energy levels of the system as a function of the frequency of qubit 1, obtained by numerical diagonalization of the Hamiltonian in Eq. (4) with four qubits. The transition frequencies of the other three qubits as well as the resonance frequency of the cavity mode are kept fixed. All the parameters used are provided in the text.
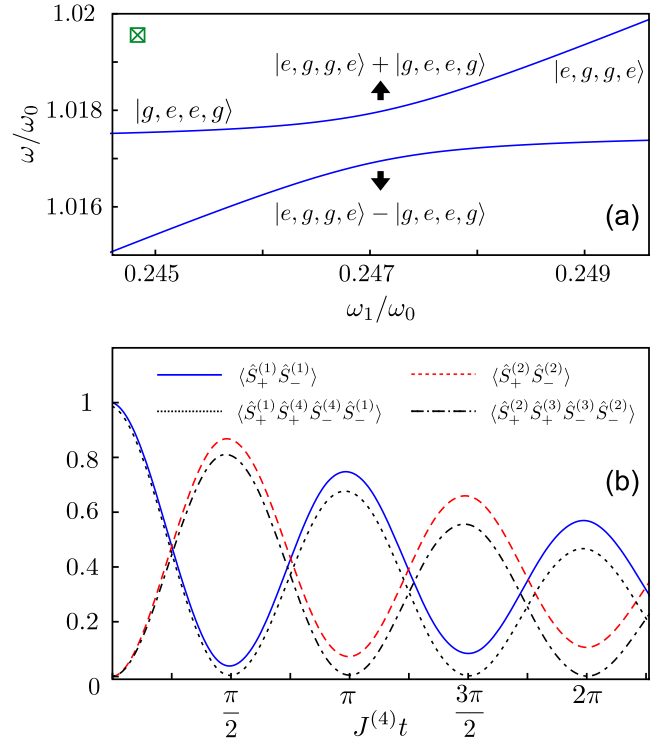

FIG. 5. (a) Enlarged view of the *apparent* crossing (⊠) in Fig. 4 determining a type-I 4QM. (b) Type-I 4QM: Time evolution of the mean excitation probability of qubits 1 and 2, $\langle \hat{S}_+^{(1)} \hat{S}_-^{(1)} \rangle$ and $\langle \hat{S}_+^{(2)} \hat{S}_-^{(2)} \rangle$, and of the two-qubit correlation functions $\langle \hat{S}_+^{(1)} \hat{S}_+^{(4)} \hat{S}_-^{(4)} \hat{S}_-^{(1)} \rangle$ and $\langle \hat{S}_+^{(2)} \hat{S}_+^{(3)} \hat{S}_-^{(3)} \hat{S}_-^{(2)} \rangle$. The initial state is $|e,g,g,e,0\rangle$.

Also in this case, the origin of this coupling can be understood using time-dependent fourth-order perturbation theory, using Eq. (7) and considering the states $|e,g,g,e,0\rangle_b$ and $|g,e,e,g,0\rangle_b$ as the initial and final states (see Appendix C). We notice that type-I 4QM, in contrast to the 3QM process, conserves the number of excitations. Hence we can expect that it can be described within the RWA (for the TC model). However, by numerically diagonalizing the TC model we find no avoided level splitting. As shown in Appendix C, the fourth-order perturbation theory shows that the coupling goes to zero, owing to perfect cancellation between the different contributions to the matrix element. This 4QM process can be described by the effective interaction Hamiltonian in Eq. (3), which determines the coupling between the states $|g,g,e,e,0\rangle$ and $|e,e,g,g,0\rangle$.

Figure 5(b) displays the time evolution of the mean excitation probability of qubits 1 and 2 (the dynamics of qubits 3 and 4 coincide with that of qubits 1 and 2, respectively), as well as that of the two-qubit correlation functions $\langle \hat{S}_+^{(1)} \hat{S}_+^{(4)} \hat{S}_-^{(4)} \hat{S}_-^{(1)} \rangle$ and $\langle \hat{S}_+^{(2)} \hat{S}_+^{(3)} \hat{S}_-^{(3)} \hat{S}_-^{(2)} \rangle$. The parameters are those used to obtain the energy levels in Fig. 4. We also set $\gamma = \kappa = 3 \times 10^{-5} \omega_0$. The initial state is $|e,g,g,e,0\rangle$. The system can be prepared in this state by setting the qubit frequencies such that $\omega_1 + \omega_4 \neq \omega_2 + \omega_3$ and directly exciting qubits 1 and 4 by sending a π pulse to each of them, followed by a flux shift to one of the four qubits that brings the four-qubit system into resonance [corresponding to the minimum splitting in Fig. 5(a)]. At $t = 0$,

qubits 1 and 4 are excited and the minimum-splitting condition is satisfied. Figure 5(b) clearly demonstrates the excitation transfer $|e,g,g,e,0\rangle \rightarrow |g,e,e,g,0\rangle$, which is also reversible as the time evolution for $\pi/2 \leqslant J^{(4)} t \leqslant \pi$ shows. If damping is absent or negligible, the transfer can be deterministic at $J^{(4)} t = \pi/2$, and a maximally entangled four-qubit state (GHZ-type state) is obtained at $J^{(4)} t = \pi/4$.

This 4QM process can be used to transfer the entanglement from a pair of qubits to another spatially separated pair, initially in a factorized state. Specifically, if the system is initially prepared in the two-qubit entangled state $(a|g,g\rangle + b|e,e\rangle)|g,g\rangle$, after a time $t = \pi/2J^{(4)}$, the entanglement will be transferred from qubits 1 and 2 to qubits 3 and 4: $(a|g,g\rangle + b|e,e\rangle)|g,g\rangle \rightarrow |g,g\rangle(a|g,g\rangle - ib|e,e\rangle)$.

Adjusting the transition frequencies of the qubits, a four-qubit down-conversion (type-II 4QM) analogous to that studied above for three qubits can also occur. This process is enabled by the resonant coupling between the states $|e,g,g,g,0\rangle \leftrightarrow |g,e,e,e,0\rangle$ and can be described by the effective Hamiltonian

$$\hat{V}_{\mathrm{II}}^{(4)} = J^{(4)} (\hat{\sigma}_-^{(1)} \hat{\sigma}_+^{(2)} \hat{\sigma}_+^{(3)} \hat{\sigma}_+^{(4)} + \mathrm{H.c.}). \tag{10}$$

As shown in Appendix A, the resulting splitting is of the same order as that shown in Fig. 5(a). The spontaneous evolution of the Dicke USC system, effectively described by the Hamiltonian (10), corresponding to a type-II 4QM,
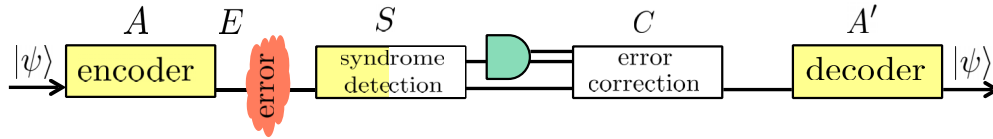
FIG. 6. Basic modules of a standard ECC. These include encoding (A) and decoding (A') modules (usually based on quantum repetition codes using multiple CNOT gates), a dissipative channel or evolution when the error (E) happens, error-syndrome detection (S), and error-correction (C) modules. Sometimes, the modules S and C are combined. Here, single (double) lines denote quantum (classical) channels, and a half-circle denotes detectors. In Appendix D, we consider in detail an ECC (see, e.g., Ref. [41]) for correcting either a single bit-flip or single phase-flip error. Then, modules A and A' can be entirely implemented (as marked in yellow) by a type-II 4QM, described by $\hat{V}_{II}^{(4)}$ for the evolution time (length) $t' = \pi/(2J^{(4)})$. Typically, modules A and A' are realized with four CNOT gates in total. Moreover, the error-syndrome module S can be implemented by 4QM and two additional CNOT gates, instead of typically four CNOT gates. The detected error can be corrected by a single-qubit rotation (NOT gate) applied to a proper qubit, based on the results of the detectors, as discussed in Appendix D.

performs the transformation

$$(a|g\rangle + b|e\rangle)|ggg\rangle \rightarrow |g\rangle(a|ggg\rangle - ib|eee\rangle) \qquad (11)$$

after the evolution time $t' = \pi/(2J^{(4)})$. This operation corresponds, up to a single-qubit phase gate, to a three-qubit repetition code, which is usually implemented with two controlled-NOT (CNOT) gates. Repetition codes are basic elements of error-correction codes (ECCs) [40,58], in particular, for encoding A and decoding A', as shown and explained in Fig. 6. Note that the error E can be corrected in the module C by a single qubit flip conditioned on the classical information obtained from the detectors in the module S. In Appendix D, we analyze in detail an ECC [41] for correcting either a single bit-flip or phase-flip error. In this ECC, a type-II 4QM can be used for three purposes: to implement encoding A and decoding A', but also to replace two CNOT gates in the error-syndrome-detection module S (see the modules depicted in yellow in Fig. 6). We note that CNOT-based ECCs (including the double-controlled-NOT gate, i.e., the Toffoli gate) were first implemented experimentally in a liquid NMR system [59] and, later, with trapped ions [60,61], linear optics [62], homogenous [63] and heterogeneous [64] solid-state spin systems, and a circuit-QED system [65–68]. Usually, the CNOT and Toffoli gates are realized by long sequences of pulses or using qudits instead of qubits [65,69]. In our proposal, the total number of eight CNOT gates in the five-qubit ECC is reduced from eight to only two, and we are not using the Toffoli gate.

Finally, we note that any entangling operation (like the type-II 4QM) is universal for quantum computing [58]. Specifically, by using many copies of such a gate together with single-qubit operations, an arbitrary quantum algorithm (i.e., not only the ECC) can be performed. However, here we focus on a direct and simple application of the spontaneous evolution of the Dicke system. Thus, we do not express the two remaining CNOT gates for the syndrome detection S via a sequence of 4QM and single-qubit operations.

III. CONCLUSIONS

In this article, we described nonlinear optical processes with qubits, where only virtual photons are involved. The results presented here show that N spatially separated and nonde- generate qubits can coherently exchange energy in analogy with light modes in nonlinear optics. The energy exchange is also reversible. This few-body interaction is mediated by the exchange of virtual rather than real photons and is protected against photon losses in the bus. The coherent coupling between the N superconducting qubits can be switched on or off by tuning the transition energy of one of them. These results can be regarded as the generalization to $N > 2$ qubits of the two-qubit coherent state transfer mediated by virtual photons experimentally demonstrated with superconducting artificial atoms [3].

These processes can produce multiparticle entanglement simply starting from one or more qubits in their excited state and letting the system evolve spontaneously. The spontaneous time evolution is also able to transfer the entanglement from one pair of qubits to a different one. The processes proposed here extend further the broad field of nonlinear optics. This architecture can be extended to consider qubits in different coupled cavities and opens up new possibilities for quantum-information processing on a chip. As an example, we have demonstrated that four-qubit mixing can be used as a replacement for the standard quantum repetition codes based on CNOT gates. Then, we have discussed a practical application of type-II four-qubit mixing for quantum-information processing, i.e., an error-correction code for encoding, decoding, and error-syndrome detection, as shown in Fig. 12 and discussed in detail in Appendix D. Finally, we observe that these effective three- and four-body interactions can give rise to exotic phases not seen in usual condensed-matter experiments [70].
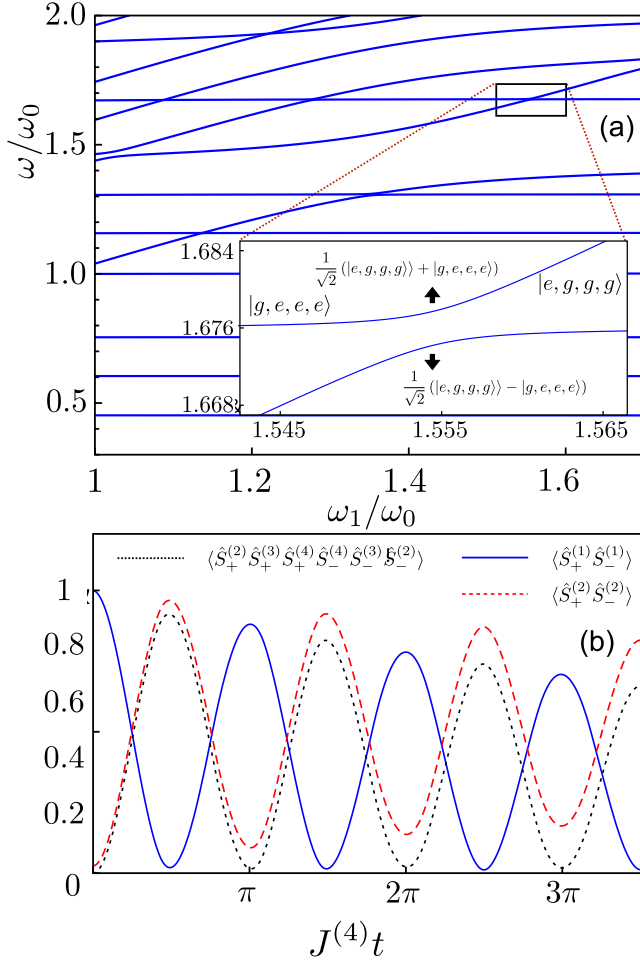
FIG. 7. Type-II 4QM. (a) Lowest-energy levels of the system constituted by four qubits interacting with a cavity mode as a function of the normalized frequency of qubit 1, obtained by numerically diagonalizing the Hamiltonian in Eq. (4). We used the following parameters in units of ω_0: $\omega_2 = 0.4$, $\omega_3 = 0.55$, $\omega_4 = 0.7$, $\omega_c = 1.75$, $\lambda_1 = 0.05$, $\lambda_i = 0.15$ (for $i = 2$–4), and $\theta_i = \pi/6$ for all four qubits. The enlarged view of the boxed *apparent* crossing in the inset displays a clear anticrossing level splitting. When the splitting is at its minimum, the eigenstates of the system are approximately symmetric and antisymmetric superpositions of the states $|e,g,g,g,0\rangle$ and $|g,e,e,e,0\rangle$. (b) Time evolution of the mean excitation probabilities of qubits 1 and 2, and of the three-qubit correlation function $\langle \hat{S}_+^{(2)} \hat{S}_+^{(3)} \hat{S}_+^{(4)} \hat{S}_-^{(4)} \hat{S}_-^{(3)} \hat{S}_-^{(2)} \rangle$, obtained fixing $\omega_1 = 1.6448$, so that the splitting in the inset is minimum. The initial state is $|e,g,g,g,0\rangle$ and we used $\gamma = \kappa = 3 \times 10^{-5}\omega_0$.

APPENDIX A: ENERGY LEVELS AND DYNAMICS FOR TYPE-II FOUR-QUBIT MIXING

Figure 7 presents the numerical calculations for type-II 4QM. Figure 7(a) displays the lowest-energy levels as a function of the normalized frequency of qubit 1, obtained by numerically diagonalizing the Hamiltonian in Eq. (4). Parameters are provided in the figure caption. Figure 7(a) also shows the enlarged view of the boxed *apparent* crossing. Figure 7(b) shows the time evolution of the mean excitation probabilities of qubits 1 and 2, and of the three-qubit correlation function $\langle \hat{S}_+^{(2)} \hat{S}_+^{(3)} \hat{S}_+^{(4)} \hat{S}_-^{(4)} \hat{S}_-^{(3)} \hat{S}_-^{(2)} \rangle$, obtained fixing $\omega_1 = 1.6448$, so that

the splitting in the inset in Fig. 7(a) is minimum. The initial state is $|e,g,g,g,0\rangle$.

APPENDIX B: ANALYTICAL DERIVATION OF THE THREE-QUBIT COUPLING STRENGTH $J^{(3)}$

Our system consists of three qubits, all ultrastrongly coupled to a cavity mode. The Hamiltonian for the system is given in Eq. (4). In this appendix, we calculate the effective 3QM coupling strength $J^{(3)}$ between the two states $|i\rangle = |e,g,g,0\rangle$ and $|f\rangle = |g,e,e,0\rangle$ (equivalent to the 3QM $|g,g,e,0\rangle \leftrightarrow |e,e,g,0\rangle$, discussed in the main text, with a permutation of the qubit indices). These states are connected via 48 fourth-order paths, as shown in Fig. 8.

We can treat the interaction part of the Hamiltonian, given in Eq. (5), as a perturbation. As discussed in the main text, the effective coupling is then given by Eq. (7), where the sum goes over all paths shown in Fig. 8. There are no contributions from terms of order lower than four. Note that $E_i = E_f = 0$ when $\omega_1 = \omega_2 + \omega_3$, which is the case considered here.

In the rest of this appendix, for brevity, we use the notation $\Delta_{nm} = \omega_n - \omega_m$, $\Delta_{Cn} = 2\omega_c - \omega_n$, $\Omega_{nm} = \omega_n + \omega_m$, $\Omega_{Cn} = 2\omega_c + \omega_n$, $\lambda_{\pm\pm\pm} = \pm\lambda_1 \pm \lambda_2 \pm \lambda_3$, $\Lambda_3 = \lambda_1\lambda_2\lambda_3$, and $\Lambda_4 = \lambda_1\lambda_2\lambda_3\lambda_4$. With this notation, the contribution from the terms in diagram 1 of Fig. 8 becomes

$$\lambda_{\text{eff}}^{(1)} = -\frac{\Lambda_3 \sin\theta \cos^3\theta}{\Delta_{c1}}\left[2\frac{\lambda_{-++}}{\omega_c\Delta_{C3}} + 2\frac{\lambda_{-+-}}{\Delta_{C2}\Delta_{c3}}\right.$$
$$+ 2\frac{\lambda_{-++}}{\omega_c\Delta_{C2}} + 2\frac{\lambda_{--+}}{\Delta_{C2}\Delta_{c2}} + 2\frac{\lambda_{---}}{\Delta_{C1}\Delta_{c3}} + 2\frac{\lambda_{---}}{\Delta_{C1}\Delta_{c1}}$$
$$+ \frac{\lambda_{-++}}{\omega_c(-\omega_3)} + \frac{\lambda_{-+-}}{(-\omega_1)\Delta_{c1}} + \frac{\lambda_{-++}}{\omega_c(-\omega_2)} + \frac{\lambda_{--+}}{(-\omega_2)\Delta_{c2}}$$
$$\left.+ \frac{\lambda_{---}}{(-\omega_1)\Delta_{c3}} + \frac{\lambda_{---}}{(-\omega_1)\Delta_{c2}}\right]. \tag{B1}$$

To check our calculations, we can compare with the calculation in Ref. [35], which treated the process $|g,g,1\rangle \rightarrow |e,e,0\rangle$. This is exactly the process in diagram 1 after the first transition, ignoring the first qubit. If we insert the values $\omega_c = 2\omega_q$, $\omega_2 = \omega_3 = \omega_0$, $\omega_1 = 2\omega_0$ [recall that we have used the fact that $\omega_1 = \omega_2 + \omega_3$ to derive Eq. (B1)], $\lambda_2 = \lambda_3 = \lambda$, and $\lambda_1 = 0$ in Eq. (B1), and remove the factor $-\lambda_1 \cos\theta/\Delta_{c1}$ (which comes from the first transition in the diagram), we obtain

$$\lambda_{\text{eff}}^{(1\text{ph},2\text{qb})} = -\frac{8}{3}\sin\theta\cos^2\theta\frac{\lambda^3}{\omega_0^2}, \tag{B2}$$

which is exactly the result from Ref. [35].

If we make the simplifying assumptions $\lambda_1 = \lambda_2 = \lambda_3 \equiv \lambda$, $\omega_1 \equiv \omega_0$, and $\omega_2 = \omega_3 = \omega_0/2$, the contribution from diagram 1 to the coupling becomes

$$\lambda_{\text{eff}}^{(1)} = -\frac{2\lambda^4 \sin\theta\cos^3\theta}{\omega_c - \omega_0}\left[\frac{2}{\omega_c(2\omega_c - \frac{1}{2}\omega_0)}\right.$$
$$- \frac{2}{(\omega_c - \frac{1}{2}\omega_0)(2\omega_c - \frac{1}{2}\omega_0)} - \frac{12}{(2\omega_c - \omega_0)^2}$$
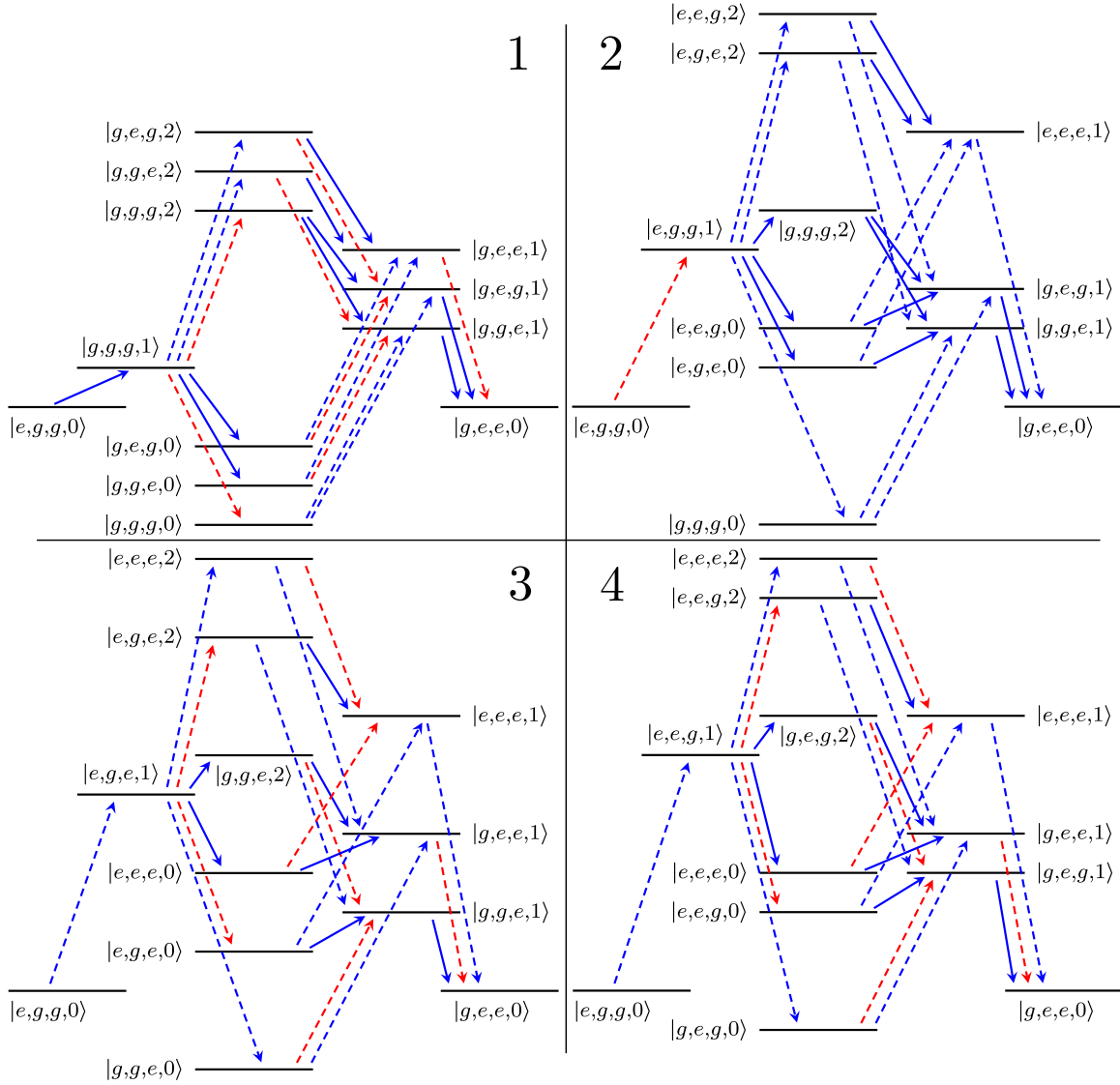$$\left.- \frac{2}{\omega_c\omega_0} + \frac{5}{\omega_0(\omega_c - \frac{1}{2}\omega_0)}\right]. \tag{B3}$$

FIG. 8. The 48 fourth-order paths connecting the states $|e,g,g,0\rangle$ and $|g,e,e,0\rangle$. The four diagrams show 12 paths each. Diagram 1 shows the paths starting with $|e,g,g,0\rangle \rightarrow |g,g,g,1\rangle$, diagram 2 shows the paths starting with $|e,g,g,0\rangle \rightarrow |e,g,g,1\rangle$, diagram 3 shows the paths starting with $|e,g,g,0\rangle \rightarrow |e,g,e,1\rangle$, and diagram 4 shows the paths starting with $|e,g,g,0\rangle \rightarrow |e,e,g,1\rangle$. Transitions that do not conserve the number of excitations in the system are marked by dashed lines, while transitions that conserve the number of excitations are marked by solid lines. The red lines mark the transitions mediated by the $\hat{\sigma}_z$ part of the coupling and the blue lines mark the transitions mediated by the $\hat{\sigma}_x$ part of the coupling. To set the energy levels, we have used the parameter values $\omega_c = 4\omega_3$, $\omega_1 = 3\omega_3$, and $\omega_2 = 2\omega_3$.

The terms from diagram 2 add up to

$$\lambda_{\text{eff}}^{(2)} = -\frac{\Lambda_3 \lambda_{+--} \sin\theta \cos^3\theta}{\omega_c}\left[\frac{2}{\Omega_{C2}\Omega_{c1}} + \frac{2}{\Omega_{C2}\Delta_{c3}} + \frac{2}{\Omega_{C3}\Omega_{c1}} + \frac{2}{\Omega_{C3}\Delta_{c2}} + \frac{2}{\Delta_{C1}\Delta_{c3}} + \frac{2}{\Delta_{C1}\Delta_{c2}} + \frac{1}{\omega_2\Omega_{c1}} + \frac{1}{\omega_2\Delta_{c3}}\right.$$

$$\left. + \frac{1}{\omega_3\Omega_{c1}} + \frac{1}{\omega_3\Delta_{c2}} + \frac{1}{(-\omega_1)\Delta_{c3}} + \frac{1}{(-\omega_1)\Delta_{c2}}\right], \tag{B4}$$

and with the same assumptions as above ($\lambda_1 = \lambda_2 = \lambda_3 \equiv \lambda$, $\omega_1 \equiv \omega_0$, and $\omega_2 = \omega_3 = \omega_0/2$) this simplifies to

$$\lambda_{\text{eff}}^{(2)} = \frac{2\lambda^4 \sin\theta \cos^3\theta}{\omega_c}\left[\frac{2}{(2\omega_c + \frac{1}{2}\omega_0)(\omega_c + \omega_0)} + \frac{2}{(2\omega_c + \frac{1}{2}\omega_0)(\omega_c - \frac{1}{2}\omega_0)} + \frac{4}{(2\omega_c - \omega_0)^2} + \frac{2}{\omega_0(\omega_c + \omega_0)}\right.$$

$$\left. + \frac{1}{\omega_0(\omega_c - \frac{1}{2}\omega_0)}\right]. \tag{B5}$$

The terms from diagram 3 add up to

$$\lambda_{\text{eff}}^{(3)} = -\frac{\Lambda_3 \sin\theta \cos^3\theta}{\Omega_{c3}} \left[2\frac{\lambda_{+++}}{\Omega_{C1}\Omega_{c1}} + 2\frac{\lambda_{-++}}{\Omega_{C1}\omega_c} + 2\frac{\lambda_{+-+}}{\Omega_{C3}\Omega_{c1}} + 2\frac{\lambda_{+-+}}{\Omega_{C3}\Delta_{c2}} + 2\frac{\lambda_{-++}}{\Delta_{C2}\omega_c} + 2\frac{\lambda_{--+}}{\Delta_{C2}\Delta_{c2}} + \frac{\lambda_{+++}}{\omega_1\Omega_{c1}} \right.$$
$$\left. + \frac{\lambda_{-++}}{\omega_1\omega_c} + \frac{\lambda_{+-+}}{\omega_3\Omega_{c1}} + \frac{\lambda_{+-+}}{\omega_3\Delta_{c2}} + \frac{\lambda_{-++}}{(-\omega_2)\omega_c} + \frac{\lambda_{--+}}{(-\omega_2)\Delta_{c2}} \right], \tag{B6}$$

and with the same assumptions as above this simplifies to

$$\lambda_{\text{eff}}^{(3)} = -\frac{\lambda^4 \sin\theta \cos^3\theta}{\omega_c + \frac{1}{2}\omega_0} \left[\frac{6}{(2\omega_c + \omega_0)(\omega_c + \omega_0)} + \frac{2}{(2\omega_c + \omega_0)\omega_c} + \frac{2}{(2\omega_c + \frac{1}{2}\omega_0)(\omega_c + \omega_0)} + \frac{2}{(2\omega_c + \frac{1}{2}\omega_0)(\omega_c - \frac{1}{2}\omega_0)} \right.$$
$$\left. + \frac{2}{(2\omega_c - \frac{1}{2}\omega_0)\omega_c} - \frac{2}{(2\omega_c - \frac{1}{2}\omega_0)(\omega_c - \frac{1}{2}\omega_0)} + \frac{5}{\omega_0(\omega_c + \omega_0)} - \frac{1}{\omega_0\omega_c} + \frac{4}{\omega_0(\omega_c - \frac{1}{2}\omega_0)} \right]. \tag{B7}$$

The terms from diagram 4 add up to $\lambda_{\text{eff}}^{(4)}$, which is given by Eq. (B6) but with the indices 2 and 3 interchanged everywhere. With the same assumptions as above $\lambda_{\text{eff}}^{(4)}$ simplifies to exactly the same expression as for diagram 3, given in Eq. (B7). Adding up all the terms from the four diagrams in the simplified case gives

$$\lambda_{\text{eff}} = -2\lambda^4 \sin\theta \cos^3\theta \left\{ \frac{1}{\omega_c - \omega_0} \left[\frac{2}{\omega_c(2\omega_c - \frac{1}{2}\omega_0)} - \frac{2}{(2\omega_c - \frac{1}{2}\omega_0)(\omega_c - \frac{1}{2}\omega_0)} - \frac{12}{(2\omega_c - \omega_0)^2} \right. \right.$$
$$\left. - \frac{2}{\omega_c\omega_0} + \frac{5}{(\omega_c - \frac{1}{2}\omega_0)\omega_0} \right] - \frac{1}{\omega_c} \left[\frac{2}{(2\omega_c + \frac{1}{2}\omega_0)(\omega_c + \omega_q)} + \frac{2}{(2\omega_c + \frac{1}{2}\omega_0)(\omega_c - \frac{1}{2}\omega_0)} \right.$$
$$\left. + \frac{4}{(2\omega_c - \omega_0)^2} + \frac{2}{\omega_0(\omega_c + \omega_0)} + \frac{1}{\omega_0(\omega_c - \frac{1}{2}\omega_0)} \right] + \frac{1}{\omega_c + \frac{1}{2}\omega_0} \left[\frac{6}{(2\omega_c + \omega_0)(\omega_c + \omega_0)} \right.$$
$$+ \frac{2}{(2\omega_c + \omega_0)\omega_c} + \frac{2}{(2\omega_c + \frac{1}{2}\omega_0)(\omega_c + \omega_0)} + \frac{2}{(2\omega_c + \frac{1}{2}\omega_0)(\omega_c - \frac{1}{2}\omega_0)} + \frac{2}{(2\omega_c - \frac{1}{2}\omega_0)\omega_c}$$
$$\left. \left. - \frac{2}{(2\omega_c - \frac{1}{2}\omega_0)(\omega_c - \frac{1}{2}\omega_0)} + \frac{5}{\omega_q(\omega_c + \omega_0)} - \frac{1}{\omega_0\omega_c} + \frac{4}{\omega_0(\omega_c - \frac{1}{2}\omega_0)} \right] \right\}. \tag{B8}$$

We note that the part from diagram 1 gives the largest contribution, since the first transition in that diagram has a smaller energy difference than the first transitions in the other diagrams, resulting in a smaller denominator.

The expression in Eq. (B8) turns out to simplify much further when everything is put on a common denominator.
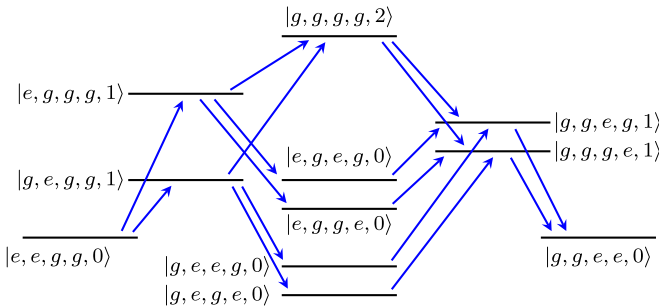

FIG. 9. The eight fourth-order paths connecting the states $|e,e,g,g,0\rangle$ and $|g,g,e,e,0\rangle$ using only the TC terms. To set the energy levels, we have used the parameter values $\omega_c = 6\omega_2$, $\omega_1 = 4\omega_2$, $\omega_3 = 3\omega_2$, and $\omega_4 = 2\omega_2$.

The final result is

$$\lambda_{\text{eff}} = J^{(3)} = \frac{64\lambda^4\omega_c^2(4\omega_c^2 - 7\omega_0^2)\sin\theta\cos^3\theta}{\omega_0(\omega_0^2 - \omega_c^2)(\omega_0^2 - 4\omega_c^2)^2}, \tag{B9}$$

which is discussed further in the main text.

We note that the coupling, also in the unsimplified case, is proportional to $\sin\theta\cos^3\theta$. Differentiating this with respect to θ and setting the derivative to zero, we obtain

$$0 = \cos^2\theta(\cos^2\theta - 3\sin^2\theta). \tag{B10}$$

Since $\cos\theta = 0$ implies $\lambda_{\text{eff}} = 0$, Eq. (B10) gives that the maximum coupling is achieved when

$$\theta = \pm\arctan\frac{1}{\sqrt{3}} = \pm\frac{\pi}{6}. \tag{B11}$$

APPENDIX C: ANALYTICAL CALCULATIONS WITH FOUR QUBITS

Our system now consists of four qubits, all ultrastrongly coupled to a cavity mode. We calculate the effective

coupling strength between the two states $|i\rangle = |e,e,g,g,0\rangle$ and $|f\rangle = |g,g,e,e,0\rangle$ (equivalent to the 4QM $|e,g,g,e,0\rangle \leftrightarrow |g,e,e,g,0\rangle$, discussed in the main text, with a permutation of the qubit indices). Since this transition conserves the total number of excitations in the system, we limit our study to the case where $\theta_i = 0$ for all four qubits in the interaction Hamiltonian Eq. (5). The Hamiltonian we work with is thus

$$\hat{H} = \omega_c \hat{a}^\dagger \hat{a} + \sum_{i=1}^{4} \frac{\omega_i}{2} \hat{\sigma}_z^{(i)} + (\hat{a} + \hat{a}^\dagger) \sum_{i=1}^{4} \lambda_i \hat{\sigma}_x^{(i)}. \quad (C1)$$

In fact, since the number of excitations is conserved, we can also consider only the TC terms in Eq. (C1), i.e., the TC

Hamiltonian

$$\hat{H} = \omega_c \hat{a}^\dagger \hat{a} + \sum_{i=1}^{4} \frac{\omega_i}{2} \hat{\sigma}_z^{(i)} + \sum_{i=1}^{4} \lambda_j \big(\hat{a}\hat{\sigma}_+^{(i)} + \hat{a}^\dagger \hat{\sigma}_-^{(i)}\big). \quad (C2)$$

The two states $|e,e,g,g,0\rangle$ and $|g,g,e,e,0\rangle$ are connected via fourth-order processes. If we use Eq. (C2), there are eight paths connecting the states to this order, as shown in Fig. 9. If we use Eq. (C1) instead, there are 48 paths connecting the states to this order, as shown in Fig. 10.

1. Calculations with the Tavis-Cummings Hamiltonian

We use the same calculation method, as well as the notation, as in Appendix B. From Eqs. (7) and (C2) and Fig. 9, we then obtain the effective coupling

$$\lambda_{\text{eff}} = -\Lambda_4 \Bigg[\frac{2}{\Delta_{c2}(\Delta_{c1} + \Delta_{c2})(\Delta_{c1} + \Delta_{32})} + \frac{2}{\Delta_{c2}(\Delta_{c1} + \Delta_{c2})(\Delta_{c1} + \Delta_{42})}$$
$$+ \frac{1}{\Delta_{c2}\Delta_{32}(\Delta_{c1} + \Delta_{32})} + \frac{1}{\Delta_{c2}\Delta_{42}(\Delta_{c1} + \Delta_{42})} + \frac{2}{\Delta_{c1}(\Delta_{c1} + \Delta_{c2})(\Delta_{c1} + \Delta_{32})}$$
$$+ \frac{2}{\Delta_{c1}(\Delta_{c1} + \Delta_{c2})(\Delta_{c1} + \Delta_{42})} + \frac{1}{\Delta_{c1}\Delta_{31}(\Delta_{c1} + \Delta_{32})} + \frac{1}{\Delta_{c1}\Delta_{41}(\Delta_{c1} + \Delta_{42})} \Bigg]$$
$$= \frac{\Lambda_4(\Delta_{13} + \Delta_{24})(\Delta_{13}\Delta_{24} + \Delta_{14}\Delta_{23})}{\Delta_{13}\Delta_{23}\Delta_{14}\Delta_{24}\Delta_{1c}\Delta_{2c}}. \quad (C3)$$

Because of the factor $\omega_1 + \omega_2 - \omega_3 - \omega_4$ in the numerator, this expression goes to zero on resonance ($\omega_1 + \omega_2 = \omega_3 + \omega_4$).

2. Calculations with the quantum Rabi Hamiltonian

The first diagram in Fig. 10 gives the following contribution to the effective coupling:

$$\lambda_{\text{eff}}^{(1)} = -\frac{\Lambda_4}{\Omega_{c3}} \Bigg[\frac{2}{(\Omega_{c3} + \Omega_{c4})(\Omega_{c3} + \Delta_{42})} + \frac{2}{(\Omega_{c3} + \Omega_{c4})(\Omega_{c3} + \Delta_{41})}$$
$$+ \frac{2}{(\Omega_{c3} + \Delta_{c2})(\Omega_{c3} + \Delta_{42})} + \frac{2}{(\Omega_{c3} + \Delta_{c2})(\Omega_{c3} - \Omega_{12})} + \frac{2}{(\Omega_{c3} + \Delta_{c1})(\Omega_{c3} + \Delta_{41})}$$
$$+ \frac{2}{(\Omega_{c3} + \Delta_{c1})(\Omega_{c3} - \Omega_{12})} + \frac{1}{\Omega_{34}(\Omega_{c3} + \Delta_{42})} + \frac{1}{\Omega_{34}(\Omega_{c3} + \Delta_{41})}$$
$$+ \frac{1}{\Delta_{32}(\Omega_{c3} + \Delta_{41})} + \frac{1}{\Delta_{32}(\Omega_{c3} - \Omega_{12})} + \frac{1}{\Delta_{31}(\Omega_{c3} + \Delta_{41})} + \frac{1}{\Delta_{31}(\Omega_{c3} - \Omega_{12})} \Bigg]. \quad (C4)$$

Note that the six last terms are just the six first terms with 2 replaced by 1 in the numerator and $2\omega_c$ replaced by zero in the denominator. This holds for all four diagrams. The terms in the second diagram contribute with

$$\lambda_{\text{eff}}^{(2)} = -\frac{\Lambda_4}{\Omega_{c4}} \Bigg[\frac{2}{(\Omega_{c3} + \Omega_{c4})(\Omega_{c3} + \Delta_{42})} + \frac{2}{(\Omega_{c3} + \Omega_{c4})(\Omega_{c3} + \Delta_{41})}$$
$$+ \frac{2}{(\Omega_{c4} + \Delta_{c2})(\Omega_{c3} + \Delta_{42})} + \frac{2}{(\Omega_{c4} + \Delta_{c2})(\Omega_{c4} - \Omega_{12})} + \frac{2}{(\Omega_{c4} + \Delta_{c1})(\Omega_{c3} + \Delta_{41})}$$
$$+ \frac{2}{(\Omega_{c4} + \Delta_{c1})(\Omega_{c4} - \Omega_{12})} + \frac{1}{\Omega_{34}(\Omega_{c3} + \omega_4 - \omega_2)} + \frac{1}{\Omega_{34}(\Omega_{c3} + \omega_4 - \omega_1)}$$
$$+ \frac{1}{\Delta_{42}(\Omega_{c3} + \Delta_{42})} + \frac{1}{\Delta_{42}(\Omega_{c4} - \Omega_{12})} + \frac{1}{\Delta_{41}(\Omega_{c3} + \Delta_{41})} + \frac{1}{\Delta_{41}(\Omega_{c4} - \Omega_{12})} \Bigg], \quad (C5)$$
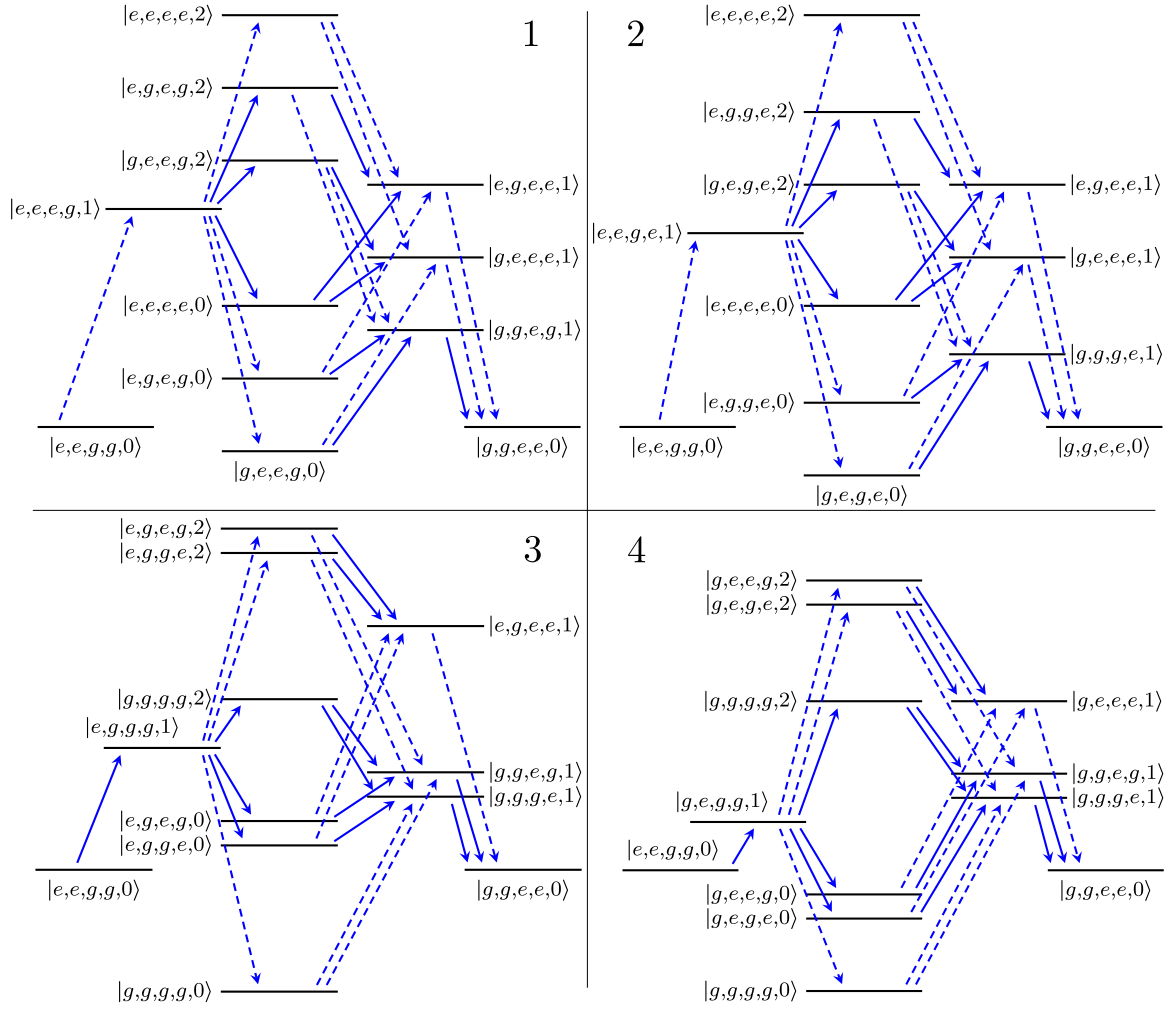
FIG. 10. The 48 fourth-order paths connecting the states $|e,e,g,g,0\rangle$ and $|g,g,e,e,0\rangle$. The four diagrams show 12 paths each. Diagram 1 shows the paths starting with $|e,e,g,g,0\rangle \rightarrow |e,e,e,g,1\rangle$, diagram 2 shows the paths starting with $|e,e,g,g,0\rangle \rightarrow |e,e,g,e,1\rangle$, diagram 3 shows the paths starting with $|e,e,g,g,0\rangle \rightarrow |e,g,g,g,1\rangle$, and diagram 4 shows the paths starting with $|e,e,g,g,0\rangle \rightarrow |g,e,g,g,1\rangle$. Transitions that do not conserve the number of excitations in the system are marked by dashed lines, while the transitions that conserve the number of excitations are marked by solid lines. To set the energy levels, we have used the same parameter values as in Fig. 9.

the terms in the third diagram give

$$\lambda_{\text{eff}}^{(3)} = -\frac{\Lambda_4}{\Delta_{c2}}\left[\frac{2}{(\Omega_{c3}+\Delta_{c2})(\Omega_{c3}+\Delta_{42})} + \frac{2}{(\Omega_{c3}+\Delta_{c2})(\Omega_{c3}-\Omega_{12})}\right.$$

$$+\frac{2}{(\Omega_{c4}+\Delta_{c2})(\Omega_{c3}+\Delta_{42})} + \frac{2}{(\Omega_{c4}+\Delta_{c2})(\Omega_{c4}-\Omega_{12})} + \frac{2}{(\Delta_{c1}+\Delta_{c2})(\Omega_{c3}-\Omega_{12})}$$

$$+\frac{2}{(\Delta_{c1}+\Delta_{c2})(\Omega_{c4}-\Omega_{12})} + \frac{1}{\Delta_{32}(\Omega_{c3}+\Delta_{42})} + \frac{1}{\Delta_{32}(\Omega_{c3}-\Omega_{12})} + \frac{1}{\Delta_{42}(\Omega_{c3}+\Delta_{42})}$$

$$\left.+\frac{1}{\Delta_{42}(\Omega_{c4}-\Omega_{12})} + \frac{1}{-\Omega_{12}(\Omega_{c3}-\Omega_{12})} + \frac{1}{-\Omega_{12}(\Omega_{c4}-\Omega_{12})}\right], \quad (C6)$$

and the terms in the fourth diagram give

$$\lambda_{\text{eff}}^{(4)} = -\frac{\Lambda_4}{\Delta_{c1}}\left[\frac{2}{(\Omega_{c3}+\Delta_{c1})(\Omega_{c3}+\Delta_{41})} + \frac{2}{(\Omega_{c3}+\Delta_{c1})(\Omega_{c3}-\Omega_{12})}\right.$$

$$+\frac{2}{(\Omega_{c4}+\Delta_{c1})(\Omega_{c3}+\Delta_{41})} + \frac{2}{(\Omega_{c4}+\Delta_{c1})(\Omega_{c4}-\Omega_{12})} + \frac{2}{(\Delta_{c1}+\Delta_{c2})(\Omega_{c3}-\Omega_{12})}$$

$$+ \frac{2}{(\Delta_{c1} + \Delta_{c2})(\Omega_{c4} - \Omega_{12})} + \frac{1}{\Delta_{31}(\Omega_{c3} + \Delta_{41})} + \frac{1}{\Delta_{31}(\Omega_{c3} - \Omega_{12})} + \frac{1}{\Delta_{41}(\Omega_{c3} + \Delta_{41})}$$

$$+ \frac{1}{\Delta_{41}(\Omega_{c4} - \Omega_{12})} + \frac{1}{-\Omega_{12}(\Omega_{c3} - \Omega_{12})} + \frac{1}{-\Omega_{12}(\Omega_{c4} - \Omega_{12})} \Bigg]. \tag{C7}$$

Adding up all these terms gives the complicated expression

$$\begin{aligned}
\lambda_{\text{eff}} = \Lambda_4 \big(\Omega_{12} - \Omega_{34}\big) &\big(3\omega_2\omega_3\omega_4\Delta_{23}\Delta_{24}\Omega_{34} + \{2\omega_c[\Delta_{23} - \omega_4] - 4\omega_c^2\}\{\omega_3^2\omega_4^2 - 3\omega_2\omega_3\omega_4\Omega_{34} + \omega_2^2[\omega_3^2 + 3\omega_3\omega_4 + \omega_4^2]\}\big] \\
&+ \omega_1^2\{\Omega_{12} - \Omega_{34} - 2\omega_c\}\{3\Delta_{23}\Delta_{24}\Omega_{34} + 2\omega_c[\omega_2^2 + \omega_3^2 + \omega_4^2 + 3\omega_3\omega_4 - 3\omega_2\Omega_{34}]\} \\
&+ \omega_1\{12\omega_c^2\Delta_{23}\Delta_{24}\Omega_{34} - 3\Delta_{23}\Delta_{24}\Omega_{34}[\omega_2\Omega_{34} - \omega_3\omega_4] \\
&+ 2\omega_c[\omega_2^2(7\omega_3^2 + 15\omega_3\omega_4 + 7\omega_4^2) + \omega_3\omega_4(3\omega_3^2 + 7\omega_3\omega_4 + 3\omega_4^2) \\
&- 3\omega_2\Omega_{34}(\omega_2^2 + \omega_3^2 + 4\omega_3\omega_4)]\}\}\big) / \Omega_{12}\Omega_{34}\Omega_{c3}\Omega_{c4}\Delta_{13}\Delta_{14}\Delta_{23}\Delta_{24}\Delta_{c1}\Delta_{c2}. \tag{C8}
\end{aligned}$$

Because of the factor $\omega_1 + \omega_2 - \omega_3 - \omega_4$ in the numerator, this expression goes to zero when $\omega_1 + \omega_2 = \omega_3 + \omega_4$. However, ω_i describe bare qubit transition frequencies. Owing to the presence of the counter-rotating terms in the atom-cavity interaction Hamiltonian, the physical transition frequencies are somewhat different from the bare ones. Hence at the physical resonance $\omega_1 + \omega_2 \neq \omega_3 + \omega_4$.

APPENDIX D: HOW TO APPLY QUBIT MIXING IN AN ERROR-CORRECTION CODE

Here we present a possible application of the spontaneous time evolution of the Dicke model, which leads to 4QM, for the qubit encoding, decoding, and error-syndrome detection modules in an ECC.

1. Quantum repetition codes via qubit mixing

As shown in Sec. II B, 4QM can occur in a system described by the Dicke model in the ultrastrong-coupling regime, which can be described by the effective Hamiltonian ($\hbar = 1$)

$$\hat{V}_{\text{II}}^{(4)} = J^{(4)} (\hat{\sigma}_-^{(1)} \hat{\sigma}_+^{(2)} \hat{\sigma}_+^{(3)} \hat{\sigma}_+^{(4)} + \text{H.c.}) \tag{D1}$$

and is referred to as type-II 4QM. The spontaneous evolution operator $\hat{U}_t$ after the time $t' = \pi/(2J^{(4)})$ is simply given by

$$\begin{aligned}
\hat{U}_{t'}^{(4)} = \exp\left(-i\hat{V}_{\text{II}}^{(4)} t'\right) = \hat{I}^{(4)} &- |0111\rangle\langle 0111| \\
&- |1000\rangle\langle 1000| - i(|0111\rangle\langle 1000| + \text{H.c.}), \tag{D2}
\end{aligned}$$

where $\hat{I}^{(4)} = \text{eye}(16)$ is the four-qubit identity operator and, for simplicity, hereafter we denote $|0\rangle \equiv |g\rangle$ and $|1\rangle \equiv |e\rangle$. Thus, an initial arbitrary state $|\psi_1\rangle = a|0\rangle + b|1\rangle$ of a single qubit and the other three qubits in the ground state $|0\rangle$ is transformed as

$$\hat{S}_4 \hat{U}_{t'}^{(4)}(a|0\rangle + b|1\rangle)|000\rangle = |0\rangle(a|000\rangle + b|111\rangle), \tag{D3}$$

as shown in Fig. 11(c). Note that the $(\pi/4)$-phase gate $\hat{S}_n = \text{diag}(1, i)$ can be applied to any qubit n except $n = 1$. It is seen that the first qubit is decoupled (disentangled) from the others at $t = 0$ and $t = t'$, so it can be discarded. Thus, Eq. (D2) effectively describes the standard ($N = 3$)-qubit

repetition code

$$\begin{aligned}
\hat{U}_{\text{rep}}^{(N)}|\psi_1\rangle|0\rangle^{\otimes(N-1)} &= \hat{U}_{\text{CNOT}}^{12} \hat{U}_{\text{CNOT}}^{13} \cdots \hat{U}_{\text{CNOT}}^{1N}|\psi_1\rangle|0\rangle^{\otimes(N-1)} \\
&= a|0\rangle^{\otimes N} + b|1\rangle^{\otimes N} \equiv |\psi_N\rangle, \tag{D4}
\end{aligned}$$

where $\hat{U}_{\text{CNOT}}^{1n}$ denotes the CNOT gate with the control (target) qubit 1 (n) for $n = 2, \ldots, N$. More precisely, $\hat{S}_4 \hat{U}_{t'}^{(4)}|\psi_1\rangle|000\rangle = (\hat{I}^{(1)} \otimes \hat{U}_{\text{rep}}^{(3)}|0\rangle|\psi_1\rangle|00\rangle$, where $\hat{I}^{(1)}$ is the single-qubit identity operator and we have an auxiliary qubit in the state $|0\rangle$ in addition to those in Eq. (D4). Analogously, it can be shown that the 3QM in the model described by the effective interaction Hamiltonian

$$\hat{V}^{(3)} = J^{(3)} (\hat{\sigma}_+^{(1)} \hat{\sigma}_+^{(2)} \hat{\sigma}_-^{(3)} + \text{H.c.}) \tag{D5}$$

after the time $t' = \pi/(2J^{(3)})$ is given by

$$\begin{aligned}
\hat{U}_{t'}^{(3)} = \exp\left(-i\hat{V}^{(3)} t'\right) = \hat{I}^{(3)} &- |011\rangle\langle 011| - |100\rangle\langle 100| \\
&- i(|011\rangle\langle 100| + \text{H.c.}), \tag{D6}
\end{aligned}$$

which realizes the two-qubit repetition code, as shown in Fig. 11(b), since

$$\hat{S}_3 \hat{U}_{t'}^{(3)}(a|0\rangle + b|1\rangle)|00\rangle = |0\rangle(a|00\rangle + b|11\rangle), \tag{D7}$$

In Eq. (D6), $\hat{I}^{(3)} = \text{eye}(8)$ is the three-qubit identity operator.

2. Error-correction code

Now we present the implementation of a toy version of an ECC (for a pedagogical description, see Ref. [41]) for correcting a single phase-flip error or a bit-flip error. We apply the ECC circuit shown in Fig. 12, and show that the quantum repetition codes, based on the CNOT gates in the modules depicted in yellow, can be replaced by the type-II 4QM described above.

Figure 11(a) shows a standard N-qubit repetition code implemented with N CNOT gates. Although CNOT gates have been implemented in circuit-QED systems, these implementations are based on a sequence of a few pulses using, usually, higher-excited levels [71,72]. Thus, it is desirable to reduce the number of CNOT gates or other entangling gates, which
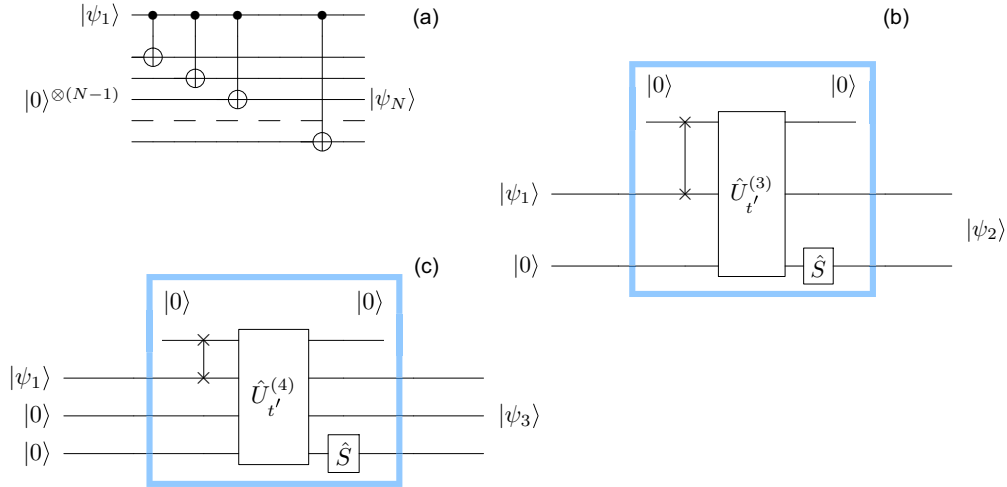
FIG. 11. (a) Standard N-qubit repetition code based on N CNOT gates for generating $|\psi_N\rangle = a|0\rangle^{\otimes N} + b|1\rangle^{\otimes N}$ (for $N = 2,3,\ldots$). Repetition codes for (b) three and (c) four qubits based on qubit mixing corresponding to the spontaneous evolution operations $\hat{U}_{t'}^{(3)}$ and $\hat{U}_{t'}^{(4)}$, given by Eqs. (D6) and (D2), respectively, followed by the $(\pi/4)$-phase gate $\hat{S}$ acting on the Nth qubit. The operation marked by $\times - \times$ corresponds to the classical SWAP gate, which is not necessary but is added to show the correspondence of all panels. In (b) and (c), the first qubit is finally disentangled from the others, so it can be discarded after the operation. In a special case, the four-qubit repetition code can implement the encoder A and decoder A', and can be used for the error-syndrome detection in the ECC shown in Fig. 12.

cannot be implemented easily like those corresponding to the spontaneous evolution of a given system.

Figure 12 shows a standard circuit implementing the ECC, which enables the correction of a single phase-flip error, or of a single bit-flip error if the blocks B and B' are omitted. These blocks B and B' are composed of three single-qubit rotations $\hat{Y}(\pi/2)$ and $\hat{Y}(-\pi/2)$ about angles of $\pm\pi/2$ around the y axis, respectively. The $\hat{Y}$ rotation about an arbitrary angle θ is defined by $\hat{Y}(\theta) = [\cos\frac{\theta}{2}, -\sin\frac{\theta}{2}; \sin\frac{\theta}{2}, \cos\frac{\theta}{2}]$. Thus, the rotations $\hat{Y}(\pm\pi/2)$ effectively realize Hadamard-like gates corresponding to rotations of the basis states $\{|0\rangle, |1\rangle\}$ into

(from) $\{|\pm\rangle = (|+\rangle + |-\rangle)/\sqrt{2}\}$ in B (B'). The modules A and B (B' and A') enable encoding (decoding) a single qubit against a single phase-flip error, while the gates A (A'), without B and B', enable encoding (decoding) a single qubit against a single bit-flip error. The module E in Fig. 12 describes a dissipative evolution or a channel, which introduces a single error (either a bit flip or a phase flip) in one of the qubits. The error-syndrome detection is performed by the four CNOT gates in the modules S_1 and S_2 using two additional qubits, which are then measured by two detectors yielding the values $m,n \in \{0,1\}$. The error correction is done in the module C
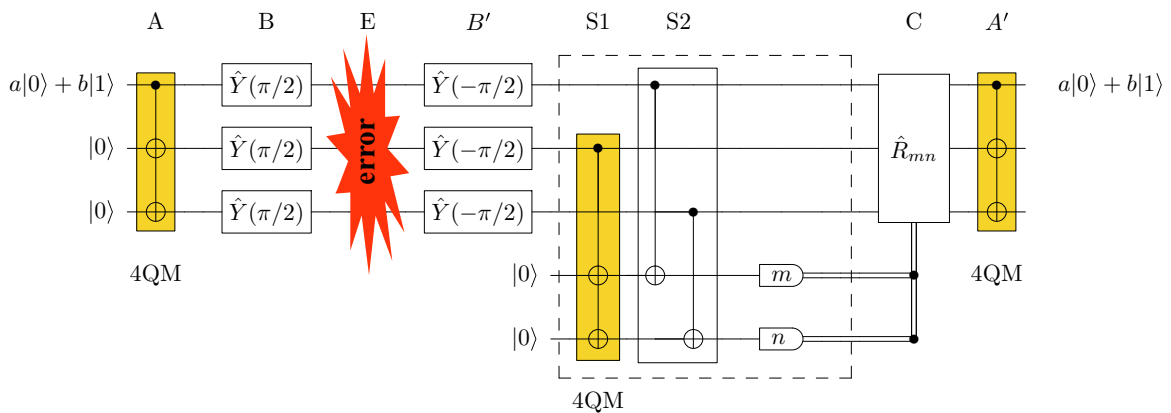

FIG. 12. Circuit implementing an ECC correcting a single phase-flip error. If the modules B and B' are omitted, then the circuit corrects a single bit-flip error. The circuit modules include encoder A, basis rotator B (from the basis $\{|0\rangle, |1\rangle\}$ into $\{|+\rangle, |-\rangle\}$) corresponding to the Hadamard gates or rotations $\hat{Y}(\pi/2)$, dissipative channel or evolution (E, when the error happens), basis rotator B' (from $\{|+\rangle, |-\rangle\}$ into $\{|0\rangle, |1\rangle\}$ being inverse to B), error-syndrome detector S (composed of blocks S_1, S_2, and detectors with two possible outcomes $m,n = 0,1$), error corrector [C, where the single-qubit operation R_{nm}, given by Eq. (D8), is conditioned on the classical information from the detectors], and decoder A'. In our implementation, the blocks A, A', and S_1, which are composed of two CNOT gates with two qubits in $|0\rangle$, can be replaced by type-II 4QM, i.e., by spontaneous evolution for the time $t = \pi/(2J^{(4)})$ of the system governed by the effective interaction Hamiltonian $\hat{V}^{(4)}$, given in Eq. (D1).

by rotating (flipping) a proper qubit as conditioned on the measured values m,n:

$$\hat{R}_{mn} = \hat{\sigma}_x^{(n-m+2)} \approx \hat{Y}_{n-m+2}(\pi), \tag{D8}$$

where we define $\hat{\sigma}_x^{(4)} \approx \hat{Y}_4(\pi)$ to be the identity operator.

As marked in yellow in Fig. 12, the encoder A, decoder A', but also the error-syndrome module S_1 can be implemented via the type-II 4QM, i.e., the spontaneous evolution of the system described by Eq. (D2). In fact, the error-syndrome module S_2 can also be expressed via the sequence of the type-II 4QM operations $\hat{U}^{(4)}$ applied to different qubits, together with single-qubit rotations. This possibility comes from the fundamental theorem about the universality of an arbitrary entangling gate (thus, including $\hat{U}^{(4)}$). However, we focus here on simple and direct applications of $\hat{U}^{(4)}$. Thus, a lengthy circuit implementing the module S_2 via $\hat{U}^{(4)}$ is not presented here.

Finally, we make three remarks:

(1) In our proposal we need to apply the 4QM between different qubits. Thus, the question arises whether one can efficiently tune the ultrastrong coupling between a chosen fraction of a collection of six qubits and a cavity field. For switching on and off the coupling it is possible to change the transition energy of the qubits involved. This can be easily done by applying, e.g., a flux offset to the qubits.

(2) By using three times the 4QM operations instead of the six CNOT gates, we need an extra qubit in addition to the five qubits shown in Fig. 11(c).

(3) In a specific physical system, it might be easier to perform 3QM rather than 4QM. Then, the six CNOT gates in the modules A, A', and S_1, shown in Fig. 11(c), can be replaced by the 3QM corresponding to the spontaneous evolution $\hat{U}_{t'}^{(3)}$, given by Eq. (D6).

[1] L. M. Duan, M. D. Lukin, J. I. Cirac, and P. Zoller, Long-distance quantum communication with atomic ensembles and linear optics, Nature (London) **414**, 413 (2001).

[2] C. W. Chou, J. Laurat, H. Deng, K. S. Choi, H. De Riedmatten, D. Felinto, and H. J. Kimble, Functional quantum nodes for entanglement distribution over scalable quantum networks, Science **316**, 1316 (2007).

[3] J. Majer, J. M. Chow, J. M. Gambetta, J. Koch, B. R. Johnson, J. A. Schreier, L. Frunzio, D. I. Schuster, A. A. Houck, A. Wallraff, A. Blais, M. H. Devoret, S. M. Girvin, and R. J. Schoelkopf, Coupling superconducting qubits via a cavity bus, Nature (London) **449**, 443 (2007).

[4] A. Gonzalez-Tudela, D. Martin-Cano, E. Moreno, L. Martin-Moreno, C. Tejedor, and F. J. Garcia-Vidal, Entanglement of Two Qubits Mediated by One-Dimensional Plasmonic Waveguides, Phys. Rev. Lett. **106**, 020501 (2011).

[5] M. Tavis and F. W. Cummings, Exact solution for an N-molecule–radiation-field Hamiltonian, Phys. Rev. **170**, 379 (1968).

[6] G. Günter, A. A. Anappara, J. Hees, A. Sell, G. Biasiol, L. Sorba, S. De Liberato, C. Ciuti, A. Tredicucci, A. Leitenstorfer, and R. Huber, Sub-cycle switch-on of ultrastrong light-matter interaction, Nature (London) **458**, 178 (2009).

[7] P. Forn-Díaz, J. Lisenfeld, D. Marcos, J. J. García-Ripoll, E. Solano, C. J. P. M. Harmans, and J. E. Mooij, Observation of the Bloch-Siegert Shift in a Qubit-Oscillator System in the Ultrastrong Coupling Regime, Phys. Rev. Lett. **105**, 237001 (2010).

[8] Y. Todorov, A. M. Andrews, R. Colombelli, S. De Liberato, C. Ciuti, P. Klang, G. Strasser, and C. Sirtori, Ultrastrong Light-Matter Coupling Regime with Polariton Dots, Phys. Rev. Lett. **105**, 196402 (2010).

[9] P. Forn-Díaz, J. J. García-Ripoll, B. Peropadre, J.-L. Orgiazzi, M. A. Yurtalan, R. Belyansky, C. M. Wilson, and A. Lupascu, Ultrastrong coupling of a single artificial atom to an electromagnetic continuum in the nonperturbative regime, Nat. Phys. **13**, 39 (2016).

[10] T. Niemczyk, F. Deppe, H. Huebl, E. P. Menzel, F. Hocke, M. J. Schwarz, J. J. García-Ripoll, D. Zueco, T. Hümmer, E. Solano, A. Marx, and R. Gross, Circuit quantum electrodynamics in the ultrastrong-coupling regime, Nat. Phys. **6**, 772 (2010).

[11] T. Schwartz, J. A. Hutchison, C. Genet, and T. W. Ebbesen, Reversible Switching of Ultrastrong Light-Molecule Coupling, Phys. Rev. Lett. **106**, 196405 (2011).

[12] G. Scalari, C. Maissen, D. Turčinková, D. Hagenmüller, S. De Liberato, C. Ciuti, C. Reichl, D. Schuh, W. Wegscheider, M. Beck, and J. Faist, Ultrastrong coupling of the cyclotron transition of a 2D electron gas to a THz metamaterial, Science **335**, 1323 (2012).

[13] M. Geiser, F. Castellano, G. Scalari, M. Beck, L. Nevou, and J. Faist, Ultrastrong Coupling Regime and Plasmon Polaritons in Parabolic Semiconductor Quantum Wells, Phys. Rev. Lett. **108**, 106402 (2012).

[14] S. Kéna-Cohen, S. A Maier, and D. D. C. Bradley, Ultrastrongly coupled exciton-polaritons in metal-clad organic semiconductor microcavities, Adv. Opt. Mater. **1**, 827 (2013).

[15] S. Gambino, M. Mazzeo, A. Genco, O. Di Stefano, S. Savasta, S. Patane, D. Ballarini, F. Mangione, G. Lerario, D. Sanvitto, and G. Gigli, Exploring light-matter interaction phenomena under ultrastrong coupling regime, ACS Photonics **1**, 1042 (2014).

[16] C. Maissen, G. Scalari, F. Valmorra, M. Beck, J. Faist, S. Cibella, R. Leoni, C. Reichl, C. Charpentier, and W. Wegscheider, Ultrastrong coupling in the near field of complementary split-ring resonators, Phys. Rev. B **90**, 205309 (2014).

[17] M. Goryachev, W. G. Farr, D. L. Creedon, Y. Fan, M. Kostylev, and M. E. Tobar, High-Cooperativity Cavity QED with Magnons at Microwave Frequencies, Phys. Rev. Appl. **2**, 054002 (2014).

[18] A. Baust, E. Hoffmann, M. Haeberlein, M. J. Schwarz, P. Eder, J. Goetz, F. Wulschner, E. Xie, L. Zhong, F. Quijandría, D. Zueco, J.-J. García-Ripoll, L. García-Álvarez, G. Romero, E. Solano, K. G. Fedorov, E. P. Menzel, F. Deppe, A. Marx, and R. Gross, Ultrastrong coupling in two-resonator circuit QED, Phys. Rev. B **93**, 214501 (2016).

[19] F. Yoshihara, T. Fuse, S. Ashhab, K. Kakuyanagi, S. Saito, and K. Semba, Superconducting qubit-oscillator circuit beyond the ultrastrong-coupling regime, Nat. Phys. **13**, 44 (2016).

[20] N. K. Langford, R. Sagastizabal, M. Kounalakis, C. Dickel, A. Bruno, F. Luthi, D. J. Thoen, A. Endo, and L. DiCarlo,

Experimentally simulating the dynamics of quantum light and matter at ultrastrong coupling, arXiv:1610.10065.

[21] Z. Chen, Y. Wang, T. Li, L. Tian, Y. Qiu, K. Inomata, F. Yoshihara, S. Han, F. Nori, J. S. Tsai, and J. Q. You, Single-photon-driven high-order sideband transitions in an ultrastrongly coupled circuit-quantum-electrodynamics system, Phys. Rev. A **96**, 012325 (2017).

[22] J. Braumüller, M. Marthaler, A. Schneider, A. Stehli, H. Rotzinger, M. Weides, and A. V. Ustinov, Analog quantum simulation of the Rabi model in the ultra-strong coupling regime, arXiv:1611.08404.

[23] S. De Liberato, D. Gerace, I. Carusotto, and C. Ciuti, Extracavity quantum vacuum radiation from a single qubit, Phys. Rev. A **80**, 053810 (2009).

[24] Q. Ai, Y. Li, H. Zheng, and C. P. Sun, Quantum anti-Zeno effect without rotating wave approximation, Phys. Rev. A **81**, 042116 (2010).

[25] R. Stassi, A. Ridolfo, O. Di Stefano, M. J. Hartmann, and S. Savasta, Spontaneous Conversion from Virtual to Real Photons in the Ultrastrong-Coupling Regime, Phys. Rev. Lett. **110**, 243601 (2013).

[26] A. Ridolfo, S. Savasta, and M. J. Hartmann, Nonclassical Radiation from Thermal Cavities in the Ultrastrong Coupling Regime, Phys. Rev. Lett. **110**, 163601 (2013).

[27] L. Garziano, A. Ridolfo, R. Stassi, O. Di Stefano, and S. Savasta, Switching on and off of ultrastrong light-matter interaction: Photon statistics of quantum vacuum radiation, Phys. Rev. A **88**, 063829 (2013).

[28] L. Garziano, R. Stassi, A. Ridolfo, O. Di Stefano, and S. Savasta, Vacuum-induced symmetry breaking in a superconducting quantum circuit, Phys. Rev. A **90**, 043817 (2014).

[29] J.-F. Huang and C. K. Law, Photon emission via vacuum-dressed intermediate states under ultrastrong coupling, Phys. Rev. A **89**, 033827 (2014).

[30] Y.-J. Zhao, Y.-L. Liu, Y.-X. Liu, and F. Nori, Generating nonclassical photon states via longitudinal couplings between superconducting qubits and microwave fields, Phys. Rev. A **91**, 053820 (2015).

[31] A. F. Kockum, V. Macrì, L. Garziano, S. Savasta, and F. Nori, Frequency conversion in ultrastrong cavity QED, Scientific Reports **7**, 5313 (2017).

[32] G. Zhu, D. G. Ferguson, V. E. Manucharyan, and J. Koch, Circuit QED with fluxonium qubits: Theory of the dispersive regime, Phys. Rev. B **87**, 024510 (2013).

[33] K. K. W. Ma and C. K. Law, Three-photon resonance and adiabatic passage in the large-detuning Rabi model, Phys. Rev. A **92**, 023842 (2015).

[34] L. Garziano, R. Stassi, V. Macrì, A. F. Kockum, S. Savasta, and F. Nori, Multiphoton quantum Rabi oscillations in ultrastrong cavity QED, Phys. Rev. A **92**, 063830 (2015).

[35] L. Garziano, V. Macrì, R. Stassi, O. Di Stefano, F. Nori, and S. Savasta, One Photon Can Simultaneously Excite Two or More Atoms, Phys. Rev. Lett. **117**, 043601 (2016).

[36] A. F. Kockum, A. Miranowicz, V. Macrì, S. Savasta, and F. Nori, Deterministic quantum nonlinear optics with single atoms and virtual photons, Phys. Rev. A **95**, 063849 (2017).

[37] L. Mandel and E. Wolf, *Optical Coherence and Quantum Optics* (Cambridge University Press, Cambridge, U.K., 1995).

[38] Y. R. Shen, *Principles of Nonlinear Optics* (Wiley-Interscience, New York, 1984).

[39] H. I. Takesue and K. Inoue, Generation of polarization-entangled photon pairs and violation of Bell's inequality using spontaneous four-wave mixing in a fiber loop, Phys. Rev. A **70**, 031802 (2004).

[40] P. W. Shor, Scheme for reducing decoherence in quantum computer memory, Phys. Rev. A **52**, R2493(R) (1995).

[41] R. T. Perry, *Quantum Computing from the Ground Up* (World Scientific, Singapore, 2012).

[42] S. L. Rolston and W. D. Phillips, Nonlinear and quantum atom optics, Nature (London) **416**, 219 (2002).

[43] G. Lenz, P. Meystre, and E. M. Wright, Nonlinear Atom Optics, Phys. Rev. Lett. **71**, 3271 (1993).

[44] M. Trippenbach, Y. Band, and P. Julienne, Four wave mixing in the scattering of Bose-Einstein condensates, Opt. Express **3**, 530 (1998).

[45] L. Deng, E. W. Hagley, J. Wen, M. Trippenbach, Y. Band, P. S. Julienne, J. E. Simsarian, K. Helmerson, S. L. Rolston, and W. D. Phillips, Four-wave mixing with matter waves, Nature (London) **398**, 218 (1999).

[46] A. Bermudez, D. Porras, and M. A. Martin-Delgado, Competing many-body interactions in systems of trapped ions, Phys. Rev. A **79**, 060303 (2009).

[47] R. H. Dicke, Coherence in spontaneous radiation processes, Phys. Rev. **93**, 99 (1954).

[48] Y. X. Liu, J. Q. You, L. F. Wei, C. P. Sun, and F. Nori, Optical Selection Rules and Phase-Dependent Adiabatic State Control in a Superconducting Quantum Circuit, Phys. Rev. Lett. **95**, 087001 (2005).

[49] J. Q. You and F. Nori, Atomic physics and quantum optics using superconducting circuits, Nature (London) **474**, 589 (2011).

[50] X. Gu, A. F. Kockum, A. Miranowicz, Y. X. Liu, and F. Nori, Microwave photonics with superconducting quantum circuits, arXiv:1707.02046.

[51] A. Blais, J. Gambetta, A. Wallraff, D. I. Schuster, S. M. Girvin, M. H. Devoret, and R. J. Schoelkopf, Quantum-information processing with circuit quantum electrodynamics, Phys. Rev. A **75**, 032329 (2007).

[52] M. Malekakhlagh, A. Petrescu, and H. E. Türeci, Cutoff-free circuit quantum electrodynamics, arXiv:1701.07935.

[53] O. Di Stefano, R. Stassi, L. Garziano, A. F. Kockum, S. Savasta, and F. Nori, Feynman-diagrams approach to the quantum Rabi model for ultrastrong cavity QED: Stimulated emission and reabsorption of virtual particles dressing a physical excitation, New J. Phys. **19**, 053010 (2017).

[54] I. Chiorescu, P. Bertet, K. Semba, Y. Nakamura, C. J. P. M. Harmans, and J. E. Mooij, Coherent dynamics of a flux qubit coupled to a harmonic oscillator, Nature (London) **431**, 159 (2004).

[55] F. Yan, S. Gustavsson, A. Kamal, J. Birenbaum, A. P. Sears, D. Hover, T. J. Gudmundsen, D. Rosenberg, G. Samach, S. Weber, J. L. Yoder, T. P. Orlando, J. Clarke, A. J. Kerman, and W. D. Oliver, The flux qubit revisited to enhance coherence and reproducibility, Nat. Commun. **7**, 12964 (2016).

[56] F. Beaudoin, J. M. Gambetta, and A. Blais, Dissipation and ultrastrong coupling in circuit QED, Phys. Rev. A **84**, 043832 (2011).

[57] A. Ridolfo, M. Leib, S. Savasta, and M. J. Hartmann, Photon Blockade in the Ultrastrong Coupling Regime, Phys. Rev. Lett. **109**, 193602 (2012).

[58] M. A. Nielsen and I. L. Chuang, *Quantum Computation and Quantum Information* (Cambridge University Press, Cambridge, U.K., 2000).

[59] D. G. Cory, M. D. Price, W. Maas, E. Knill, R. Laflamme, W. H. Zurek, T. F. Havel, and S. S. Somaroo, Experimental Quantum Error Correction, Phys. Rev. Lett. **81**, 2152 (1998).

[60] J. Chiaverini, D. Leibfried, T. Schaetz, M. D. Barrett, R. B. Blakestad, J. Britton, W. M. Itano, J. D. Jost, E. Knill, C. Langer, R. Ozeri, and D. J. Wineland, Realization of quantum error correction, Nature (London) **432**, 602 (2004).

[61] P. Schindler, J. T. Barreiro, T. Monz, V. Nebendahl, D. Nigg, M. Chwalla, M. Hennrich, and R. Blatt, Experimental repetitive quantum error correction, Science **332**, 1059 (2011).

[62] T. B. Pittman, B. C. Jacobs, and J. D. Franson, Demonstration of quantum error correction using linear optics, Phys. Rev. A **71**, 052332 (2005).

[63] O. Moussa, J. Baugh, C. A. Ryan, and R. Laflamme, Demonstration of Sufficient Control for Two Rounds of Quantum Error Correction in a Solid State Ensemble Quantum Information Processor, Phys. Rev. Lett. **107**, 160501 (2011).

[64] G. Waldherr, Y. Wang, S. Zaiser, M. Jamali, T. Schulte-Herbrüggen, H. Abe, T. Ohshima, J. Isoya, J. F. Du, P. Neumann, and J. Wrachtrup, Quantum error correction in a solid-state hybrid spin register, Nature (London) **506**, 204 (2014).

[65] M. D. Reed, L. DiCarlo, S. E. Nigg, L. Sun, L. Frunzio, S. M. Girvin, and R. J. Schoelkopf, Realization of three-qubit quantum error correction with superconducting circuits, Nature (London) **482**, 382 (2012).

[66] D. Ristè, S. Poletto, M.-Z. Huang, A. Bruno, V. Vesterinen, O.-P. Saira, and L. DiCarlo, Detecting bit-flip errors in a logical qubit using stabilizer measurements, Nat. Commun. **6**, 6983 (2015).

[67] J. Kelly, R. Barends, A. G. Fowler, A. Megrant, E. Jeffrey, T. C. White, D. Sank, J. Y. Mutus, B. Campbell, Yu Chen, Z. Chen, B. Chiaro, A. Dunsworth, I.-C. Hoi, C. Neill, P. J. J. O'Malley, C. Quintana, P. Roushan, A. Vainsencher, J. Wenner, A. N. Cleland, and J. M. Martinis, State preservation by repetitive error detection in a superconducting quantum circuit, Nature (London) **519**, 66 (2015).

[68] M. Takita, A. D. Córcoles, E. Magesan, B. Abdo, M. Brink, A. Cross, J. M. Chow, and J. M. Gambetta, Demonstration of Weight-Four Parity Measurements in the Surface Code Architecture, Phys. Rev. Lett. **117**, 210505 (2016).

[69] B. P. Lanyon, M. Barbieri, M. P. Almeida, T. Jennewein, T. C. Ralph, K. J. Resch, G. J. Pryde, J. L. O'Brien, A. Gilchrist, and A. G. White, Simplifying quantum logic using higher-dimensional Hilbert spaces, Nat. Phys. **5**, 134 (2008).

[70] X.-G. Wen, *Quantum Field Theory of Many-Body Systems: From the Origin of Sound to an Origin of Light and Electrons* (Oxford University Press, Oxford, U.K., 2004).

[71] L. DiCarlo, J. M. Chow, J. M. Gambetta, L. S. Bishop, B. R. Johnson, D. I. Schuster, J. Majer, A. Blais, L. Frunzio, S. M. Girvin, and R. J. Schoelkopf, Demonstration of two-qubit algorithms with a superconducting quantum processor, Nature (London) **460**, 240 (2009).

[72] L. DiCarlo, M. D. Reed, L. Sun, B. R. Johnson, J. M. Chow, J. M. Gambetta, L. Frunzio, S. M. Girvin, M. H. Devoret, and R. J. Schoelkopf, Preparation and measurement of three-qubit entanglement in a superconducting circuit, Nature (London) **467**, 574 (2010).